Identification of single Ru(II) ions on ceria as a highly active catalyst for abatement of NOx pollutants

Konstantin Khivantsev,[a]*† Nicholas R. Jaegers,[a]† Hristiyan A. Aleksandrov,[b]†* Inhak Song,[a] Xavier Isidro Pereira-Hernandez,[a] Jinshu Tian[a], Libor Kovarik,[a] Georgi N. Vayssilov,[b] Yong Wang[a,c*] and János Szanyi[a]†*

[a] Dr. Konstantin Khivantsev, Dr. Libor Kovarik, Dr. Nicholas R. Jaegers, Dr. InHak Song, Dr. Jinshu Tian , Dr. Xavier I. Pereira Hernandez, Dr. Yong Wang, Dr. Janos Szanyi,
Institute for Integrated Catalysis
Pacific Northwest National Laboratory
Richland, WA 99352 USA
Emails (correspondence to): Konstantin.Khivantsev@pnnl.gov, Haa@chem.uni-sofia.bg, Yong.Wang@pnnl.gov, Janos.Szanyi@pnnl.gov, † denotes equal contribution

[b] Professor Hristiyan A. Aleksandrov, Professor Georgi N. Vayssilov, Sofia University "St. Kl. Ohridski", Faculty of Chemistry and Pharmacy
J. Bourchier blvd, 1126, Sofia, Bulgaria

[c] Professor Yong Wang, Voiland School of Chemical Engineering and Bioengineering
Washington State University
Pullman, WA 99164 USA

Abstract: Atom trapping allows to prepare catalysts with atomically dispersed Ru ions anchored to the ceria support. The resulting catalysts free of expensive noble metals such as Pt, Pd, Rh (whose prices are ~8-60 times higher than Ru on the per-molar basis) with Ru loadings of only 0.25-0.5 wt% show excellent activity in industrially important catalytic NO oxidation reaction, a critical step that requires use of relatively large loadings of expensive noble metals in diesel aftertreatment systems. Ru_1/CeO_2 catalysts are stable during continuous cycling, ramping and cooling as well as presence of moisture. Furthermore, Ru_1/CeO_2 shows excellent NOx storage properties during cold start, with improved NO adsorption compared with the best described Pd/Zeolite NO adsorbers with ~2-3 times higher Pd loadings. We clarify the location of Ru(II) ions on the ceria surface and identify mechanism of NO oxidation (as well as reactive storage) using DFT calculations and in-situ DRIFTS/Mass-spectroscopy measurements. Furthermore, we show the possible applications of Ru_1/CeO_2 in gasoline engines for NO reduction by CO: only 0.1 wt% of atomically dispersed Ru is sufficient to achieve high activity at low temperatures. With the aid of excitation-modulation in-situ infra-red measurements, we uncover the elementary steps of NO reduction by CO on an atomically dispersed ceria-supported catalyst. Our study highlights the potential applicability of single-atom catalysts to industrially relevant NO and CO abatement.

Air pollution is one of the main issues to tackle in environmental science and catalysis [1-3]. Deteriorating air quality is directly related to toxic NO_x emissions, the majority of which are produced by vehicles exhaust. There clearly exists the urgent need to decrease emissions from engines and develop catalytic materials for NOx abatement based on less expensive (noble) metals with improved atom economy. NO oxidation is critical for environmental catalysis in diesel aftertreatment systems because NO_2 formation is important in lean NO_x reduction [34-38]. Furthermore, NO_2 facilitates ammonia selective catalytic reduction (SCR) (so-called "fast" SCR, with an ideal 1:1 ratio between NO and NO_2) and lean NO_x storage (in this case, NO must first be oxidized to NO_2 in order to be stored on LN traps materials). Best catalysts for NO oxidation typically contain a few wt% percent of expensive Pt and Pd [34-38]. Pt costs ~1,000 USD/ounce whereas Pd costs ~ 2,600 USD/ounce (note that Pt is approximately ~2 times heavier, so per molar basis the price is only ~1.3 higher for Pd than for Pt).

In recent decade, the so-called single-atom materials with efficient utilization of single metal atoms/ions have been introduced that may offer promising alternatives and unusual reactivities compared to traditional nanoparticle catalysts. For example, thermally stable atomically dispersed Pt materials on ceria have been prepared via atom trapping approach at 800 ºC [28-31]. We now extended this synthesis to Pd. We also turned our attention to another transition metal Ruthenium whose price is only ~300 USD per ounce and whose molecular weight is similar to that of Pd and Rh (Rh, on the other hand, costs ~20,000 USD per ounce, almost ~60 times more on the molar basis than Ru; Ru is approx ~8-10 times cheaper on per-molar basis than Pt and Pd).Taking advantage of the atom trapping approach, we prepared isolated Pd, Pt and Ru atoms on ceria in ~ equivalent molar amounts (atom loading per surface area of ceria) with 1 wt% Pt, 0.5 wt% Ru and 0.5 wt% Pd on ceria. We note that ceria materials with isolated Ru(II) have not been prepared or characterized before via the described method. We observed pronounced stabilization of ceria surface area after heating at 800 ºC and producing atomically dispersed M/Ceria materials as opposed to undoped ceria (Tab. S1). Doping ceria with these ions produces stable materials that can survive heating in air at 800 ºC in agreement with our latest findings [42]. HAADF-STEM images of Pd, Pt and Ru supported ceria materials (Fig. 1A-C) show crystalline ceria nanoparticles with no noble metal nanoparticles. In the case of Pt on ceria we can identify single Pt atoms located on the surface of ceria (Fig. 1B) However, in the case of Pd and Ru, although the contrast is poor, on sufficiently thin parts of ceria nanoparticles tilted slightly off the zone-axis (to decrease scattering from bright Ce atom columns), we could in fact identify single Ru atoms (shown by arrows on the surface of different ceria crystallites in Fig. 1C). In all 3 cases, EDS maps clearly reveal

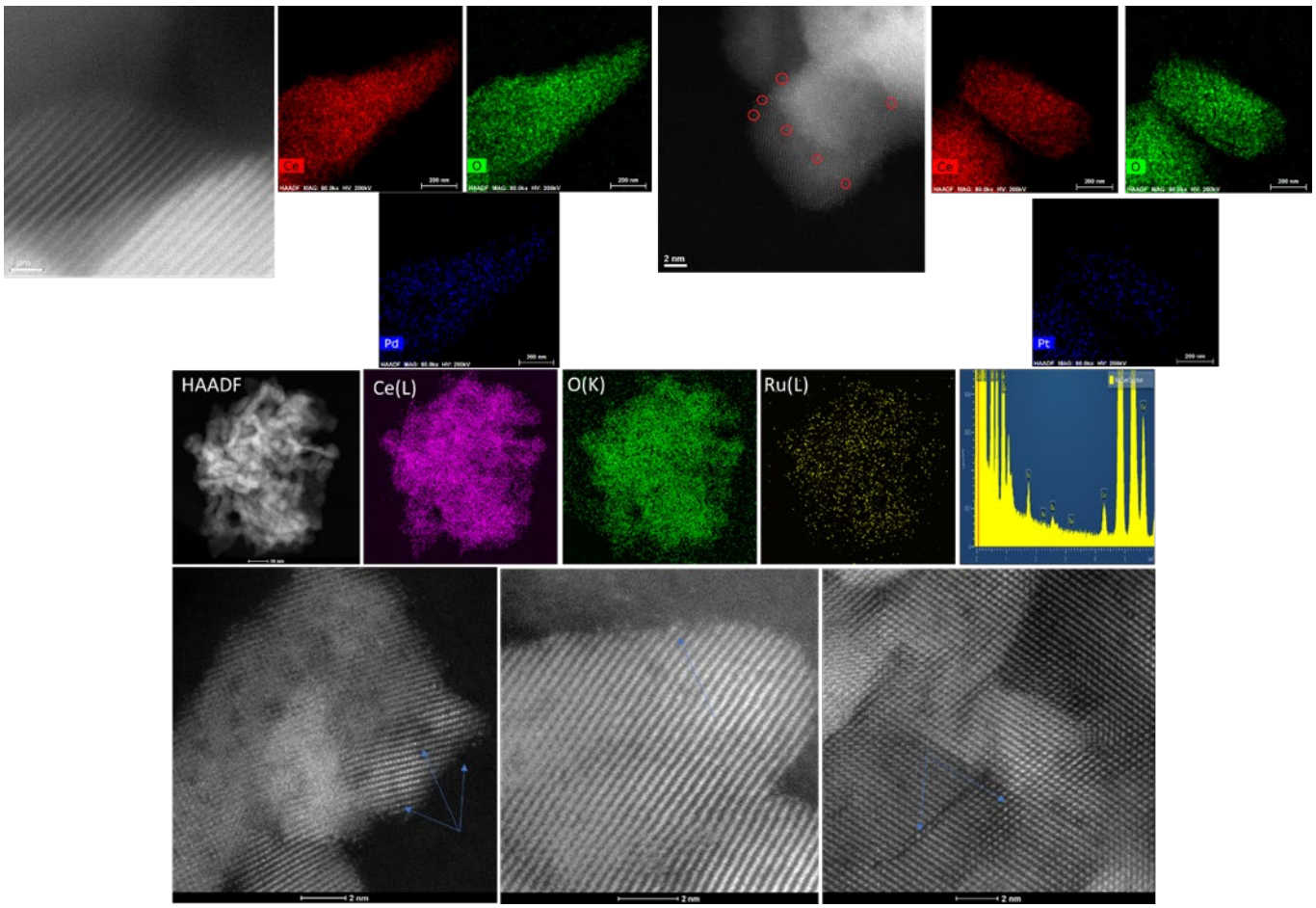

Figure 1. HAADF-STEM images and corresponding EDS maps of 0.5 wt% Pd/CeO_2, 1wt% Pt/CeO_2 and 0.5 wt% Ru/CeO_2. Single Pt and Ru atoms are highlighted with red circles and blue arrows, correspondingly.

presence of Pd, Pt and Ru well-dispersed throughout the sample, further confirming our suggestion of the atomic dispersion of the said metals on ceria. We tested these model single-atom materials for NO oxidation. Pt and Pd showed relatively low NO oxidation activities (Figs. S1,S2). To our delight, 0.5 wt% Ru/ceria sample showed excellent NO oxidation activity in the steam-containing lean $NO/O_2/N_2$ stream (Fig. 2).

The sample shows stable performance with little hysteresis going down, up and then back down in temperature (from 650 ºC to 300 ºC). Activity maximum is observed at ~345 ºC, with ~ 75% conversion of NO, comparing very favourably with commercial

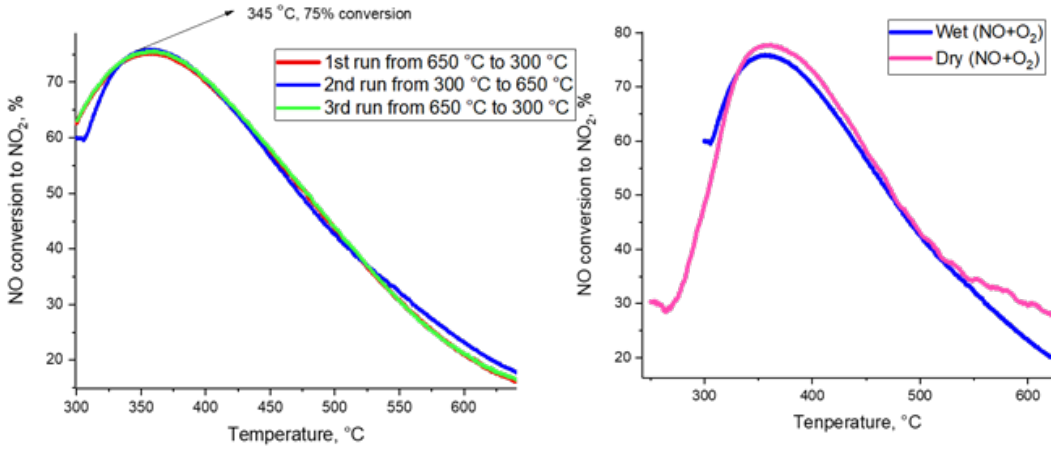

*Figure 2. NO oxidation performance of A. 0.5 wt% Ru/CeO_2(3 continuous runs from 650 to 300, 300 to 650 and then 650 to 300 ^{0}C showing stable NO oxidation performance in the presence of ~ 3% H_2O, 120 mg catalyst, 470 ppm NO, 13% O_2, total flow 300 sscm/min, GHSV ~ 150 L/g*hr. B. Comparison of wet and dry NO oxidation on aged 0.5 wt% Ru/CeO_2 going up in temperature to 650 ^{0}C (conditions are identical to A; dry experiments were carried out with the same NO and oxygen concentrations but in the absence of water)*

DOC materials tested under similar conditions [Fig. S21]. We also tested this sample in the dry NO oxidation (Fig. 2) and did not observe any prominent water influence on the NO oxidation activity. We hypothesized that this remarkable NO oxidation activity only by single-atom Ru (and not Pt and Pd) is related to the presence of labile active lattice oxygen of ceria and the ability of Ru ions to form ruthenium nitrosyl complexes. If Ru-NO complexes indeed form, then Ru-ceria should be able not to just oxidize NO but also store NO at lower temperatures: this storage is critical during vehicle cold-start and idle operation the temperatures of exhaust are lower (~100-120 ºC) and no known catalyst can catalyze NOx removal at this temperature. More specifically, Pd/zeolite formulations can store NOx at low temperatures (~100 ºC) and release them continuously > 180 ºC [7-26]. Pd is expensive and loadings of 1-2 wt% are required to achieve optimal NO adsorption. We, therefore, performed NO adsorption experiments on single-atom M/Ceria materials. Pt and Pd basically store very little NO, consistent with lack of strong bond formation between NO and Pd(II)/Pt(II) on ceria. 0.5 wt% Ru_1/CeO_2, however, showed very high NO uptake (Fig. 3) with full consumption of NO (level ~ 0 ppm) at 100 ºC.

Its performance is better than performance of Pd/SSZ-13 with ~2 times higher Pd loading (Fig. S3). NO/Ru ratio for this sample is ~2.7, showing that there is another avenue of NO storage in addition to Ru-NO complex (discussed further in the text). Hydrothermal aging at 750 °C in 10%$H_2O/O_2/N_2$ flow under simulated aging conditions does not lead to any appreciable loss of NOx storage of 0.5 wt% Ru/ceria (Fig. S4), consistent with high stability of Ru_1/CeO_2. Thus, Ru_1/CeO_2 represents an excellent NO oxidation catalyst (in the absence of Pt/Pd metals) with remarkable NO storage capacity at cold-start temperatures. We wondered if we could decrease the loading of Ru even further, while maintaining excellent NO adsorption properties and NO oxidation catalysis. We find that even at loading as low as 0.25

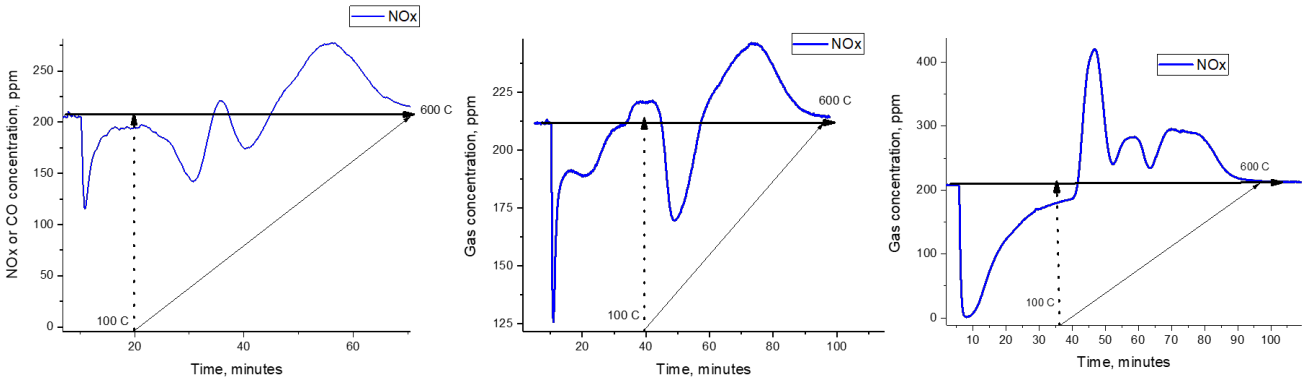

Figure 3. PNA Performance of A. 0.5 wt% Pd/CeO_2 B. 1 wt% Pt/CeO_2 C. 0.5 wt% Ru/CeO_2. Catalyst mass 120 mg. Total flow rate 300 sscm/min. ~200 ppm NOx, 13% O_2, 3% H_2O, ~200 (or 360 ppm CO) balanced in N_2. Adsorption experiments were performed at 100 °C. Vertical dashed line indicates when the ramp (10 K/min) was started.

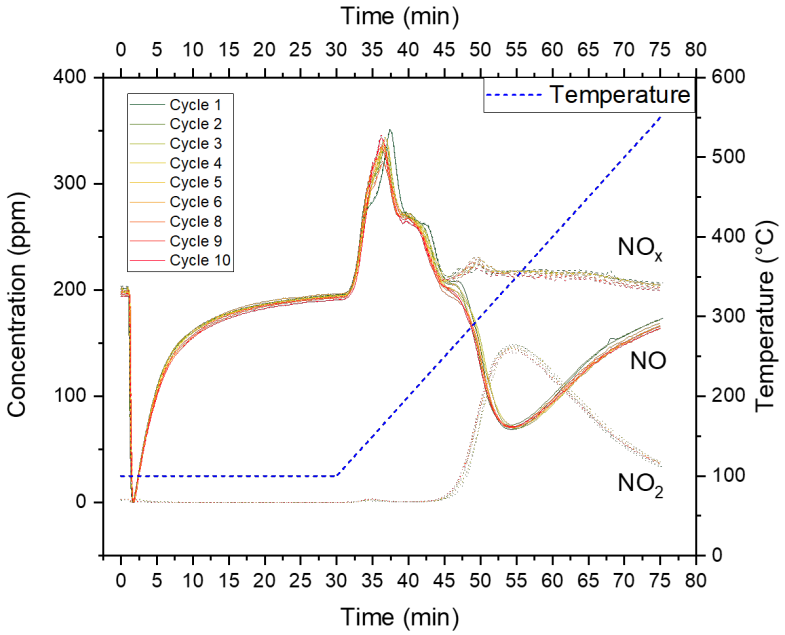

Cycle	µmol NOx	mol NOx/mol Ru
1	23.57	4.76
2	23.09	4.67
3	22.49	4.55
4	22.51	4.55
5	22.75	4.60
6	22.76	4.60
8	22.71	4.59
9	22.60	4.57
10	22.93	4.64

*Figure 4 Performance and stability of 0.25wt.% Ru_1/CeO_2 during sequential cycles of low-temperature NOx adsorption and NO oxidation. Gas composition was 200 ppm of NO, 2000 ppm CO, 12% O_2, ~3% H_2O, balanced with N_2. 120 mg catalyst was used with GHSV ~ 150 L/g*hr. Adsorption experiments were performed at 100 °C. The temperature ramp (10 °C/min) was started at a 30 minute mark; up to 550 °C. NOx storage is shown per 120 mg catalyst. On average the stored NOx amount is ~ 190 micromoles/gram.*

wt% Ru, full NO adsorption still can be achieved under simulated cold-start conditions with excellent NO oxidation activity (Fig. 4). The sample shows stable NO adsorption and NO oxidation activity evaluated continuously over 10 cycles (Figs. 4, S5). CO oxidation remains completely stable as well (Fig. S6,S7). NO oxidation activity of 750 ºC hydrothermally aged 0.25 wt% Ru_1/CeO_2 sample does not deteriorate and is comparable to the state-of-the-art industrial catalysts with ~1-2 wt% Pd (and Pt) (Fig. S21).

Ru-containing materials were studied for various catalytic processes [51,52] in the past, yet no spectroscopic investigation of single-atom Ru materials [43-46] was reported. We, therefore, studied CO and NO adsorption with infra-red spectroscopy on 0.5 wt% Ru/ceria sample. CO adsorption (Figs. S8,S9) on the sample produces no metallic CO bands for Ru and reveals the presence of $Ru(II)(CO)_2$ and $Ru(II)(CO)_3$ complexes on the surface. Adsorption of NO produces a sharp band due to NO interaction with cationic Ru at ~1,850 cm^{-1} (Fig. 5A).

in modeling ceria surface and metal-ceria interactions using state-of-the-art DFT methods can provide a molecular level insight into the precise nature and location of metal ions on ceria surfaces [60-68]. Therefore, we modelled NO complexes of Ru cations adsorbed in different locations on ceria. Five different $RuO(NO)/Ce_{21}O_{42}$ complexes were modeled (Fig. 6, Table S2). The most stable one, e-1O_NO, is obtained after adsorption of NO to the most stable $RuO/Ce_{21}O_{42}$ complex, e-1O (notation of the structures is as in Ref. 63). In this complex, where Ru center is in octahedral coordination at the small (100) facet of the $Ce_{21}O_{42}$ nanoparticle, NO donates an electron to a Ce^{4+} center, thus NO^+ ligand and a Ce^{3+} center are formed, while the formal charge of the Ru remains +2. The other structures modelled are less stable by 1.42-2.91 eV, as the formal charge of Ru is +1, since the unpaired electron is transferred from NO to the Ru center. In the structures a-1O_NO and d-1O_NO, Ru is in triangular planar coordination, interacting with two O centers and the N atom from NO. The lowest N-O vibrational frequencies were

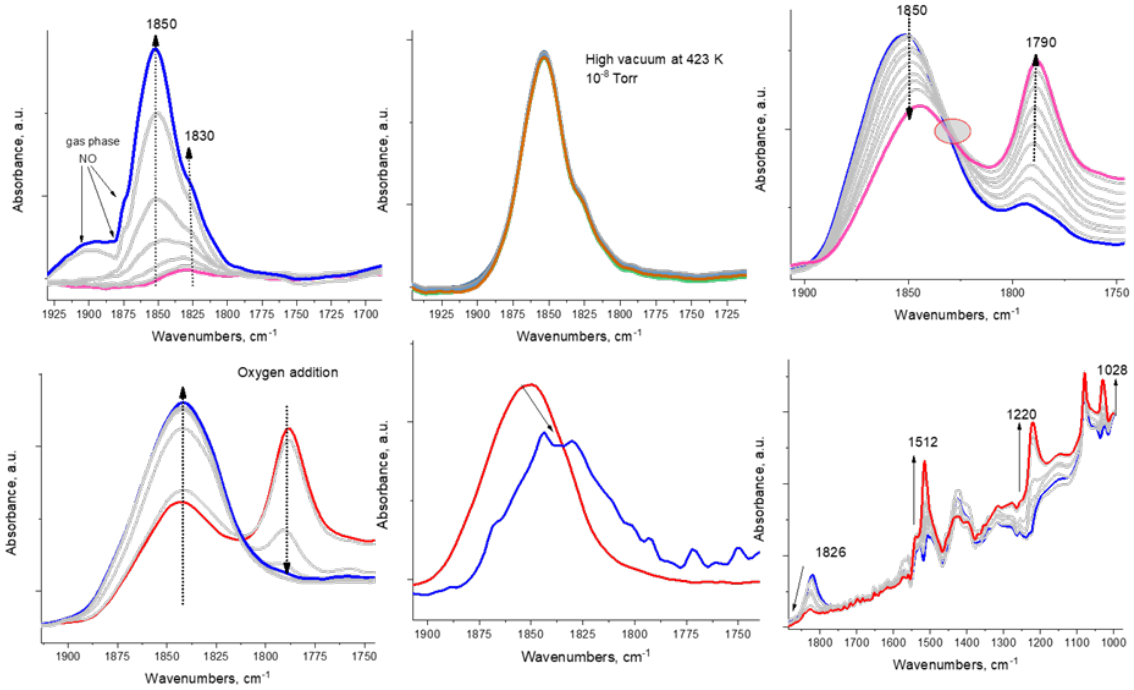

Figure 5. NO adsorption (0.5 Torr equilibrium pressure) at 298 K B. High vacuum after NO adsorption at 423 K . Heating Ru-NO from 150 to 220 ⁰C D. Introducing O_2 at 220 ⁰C after heating Ru-NO E. Water adsorption on Ru-NO complex at 120 ⁰C F Ru-NO heated in the presence of O_2+H_2O from 120 to 350 ⁰C: Ru-NO diminishes and chelating nitrates form (bands at 1512, 1220 and 1028 cm^{-1})[53].

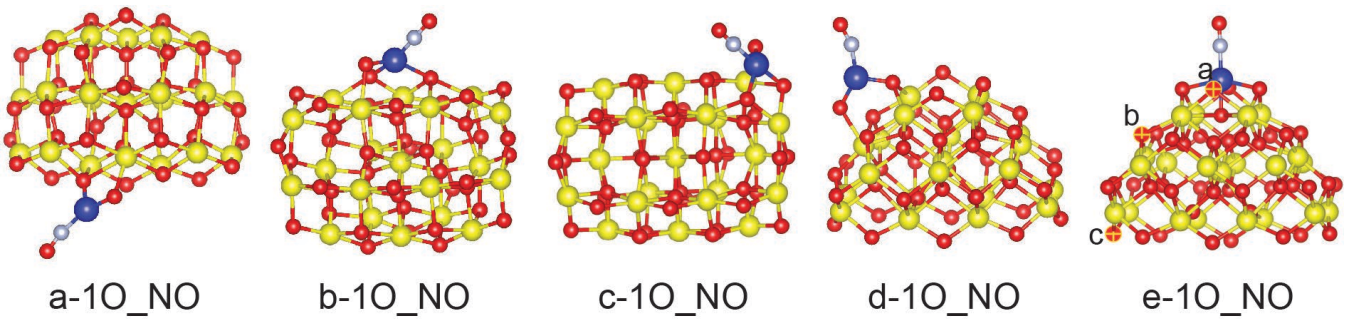

Figure 6. Optimized $RuO(NO)/Ce_{21}O_{42}$ structures. In the case of e-1O_NO complex with letters are denoted the O centers which are removed in order to obtain $RuO(NO)/Ce_{21}O_{41}$ structures. Color coding of atoms: Ce – yellow, O – red, Ru – dark blue, N – gray.

This clearly indicates the formation of a Ru-NO complex, stable even under high vacuum of ~10^{-8} Torr (Fig. 5B). Recent advances

calculated for these two structures, 1733 and 1763 cm^{-1}. Ru is in square-planar coordination in the structures b-1O_NO and c-

1O_NO, which leads to higher N-O frequencies, 1799 and 1824 cm^{-1}. The highest frequency was calculated for the most stable structure, e-1O_NO, 1840 cm^{-1}, where Ru is in octahedral coordination. This value is in excellent agreement with the experimental band at 1850 cm^{-1}. Thus, FTIR with probe molecule NO combined with state-of-the-art DFT calculations precisely identify location of active isolated Ru^{+2} cations at the small (100) facets of ceria nanoparticles in octahedral configuration.

Upon temperature increase in the absence of oxygen (Fig. 5C) this band begins to decline with a new band growing at ~ 1790 cm^{-1} and a clear isosbestic point indicating the simple stoichiometric transition of 1 Ru-NO complex into the other. We suggest that this occurs due to oxygen-vacancy formation in the vicinity of the Ru atom: ON-Ru(vac)Ce. DFT calculations further corroborate this finding. To understand this process, we modeled structures with created O vacancy from $RuO(NO)/Ce_{21}O_{42}$ complexes (Table S2). The most stable structure is e-1O_NO_vac_a, where an O center was removed from the first coordination sphere of the Ru cation. The creation of such O vacancy led to decrease of the N-O vibrational frequency from 1840 to 1788 cm^{-1} in excellent agreement with our experimental results. This is the first spectroscopic observation of the formation of an oxygen vacancy on ceria *in the direct vicinity of the metal dopant next to ceria*. Further, as soon as we add oxygen to this system, the vacancy is healed, and the NO adsorbed on Ru-O-Ce fully restores, further confirming our suggestion. This NO band is incredibly robust under high vacuum at 150 °C and does not completely disappear even at 350 °C. In the presence of water, the NO band shifts to lower wavenumbers, the phenomenon that has been previously described for Pd/SSZ-13 and Pd/ZSM-5 and due to co-coordination of water and NO to the same Pd ion [47-49]. We note, for example, that coordination of water to isoelectronic $Rh(I)(CO)_2$ and $Rh(I)(NO)_2$ complexes shifts the CO and NO bands to the lower wavenumbers . Simultaneously, in the presence of $O_2/NO/H_2O$ in the IR cell, infrared spectra emerge after running this under PNA relevant temperatures (~from 120 to 350 °C), showing the decrease of ruthenium nitrosyl complex and increase in chelating nitrate bands on the ceria surface as shown by studies of Hadjiivanov, Vayssilov and co-workers [53]. Thus, ruthenium helps store NO both as a nitrosyl complex and allows NO_x to be stored on the ceria surface due to oxidation ability (as nitrites/nitrates) explaining high NO/Ru ratio which exceeds that of NO/Pd ratio of Pd in zeolites.

We further investigated NO oxidation mechanism of Ru_1/CeO_2 using combined DRIFTS and mass spectrometry (Figs. S10-S15 show *sequential* in-situ DRIFTS and mass spectroscopy experiments that were performed).

We first performed NO adsorption in the DRIFTS flow-through cell, and the result agrees with static IR experiment: upon NO adsorption Ru-NO complex forms very fast and surface nitrites form more slowly. In the presence of oxygen, surface nitrites turn to surface nitrates at elevated temperatures. Only when the nitrates begin to decompose, mass-spec TPD with in-situ DRIFTS reveals that NO_2 begins to form (this holds true for a few continuous IR/TPD MS cycles performed. We considered the NO oxidation on $RuO/Ce_{21}O_{42}$ complexes (Table S3), considering the most stable positions for RuO species on both types of facets (100 and 111) on the $Ce_{21}O_{42}$ nanoparticle, e-1O and c-1O structures, respectively. This process includes four reaction steps: (1) oxidation of Ru species to RuO; (2) adsorption of NO to $RuO/Ce_{21}O_{42}$; (3) NO oxidation to NO_2 on Ru, as in the case of c-1O_NO complex the oxidation was considered from the additionally adsorbed in the first reaction step O center, while in the e-1O_NO complex the oxidation was done by an O center from the (100) facet; (4) NO_2 desorption from $Ru/Ce_{21}O_{42}$. The first two adsorption steps are strongly exothermic, while the oxidation and desorption are strongly endothermic. The rate-limiting step seems to be the NO oxidation, as the barriers are as high as 182 and 249 kJ/mol, respectively, on c-1O and e-1O sites. However, if all contributions to the enthalpy as well as the entropy are taken into account at temperature of 623 K, the corresponding Gibbs free barriers become 154 and 200 kJ/mol. The former barrier seems to be operative at 623 K, as the calculated kinetic constant is 1.58 s^{-1} (pre-exponential factor of the Eyring equation was taken to be 1) which corresponds to a half-life T½ of ~0.44 sec. The NO_2 desorption is strongly endothermic, but when the entropy contribution is considered the endothermicity of the process is reduced by ~150 kJ/mol, as in the case of e-1O complex it becomes even exothermic. This corresponds very well with our DRIFTS/Mass-spec data showing that NO association with interfacial Ru-O-Ce oxygen as well as nitrate decomposition steps are the legitimate pathways of NO_2 formation. The real rate constant at 623 K corresponds is ~0.015 s^{-1} per Ru site (~54 hr^{-1}). It agrees with the calculated TOF within acceptable error margin. Furthermore, it exceeds the TOF estimated for the most effective bimetallic and mono-metallic Pt and PtPd catalysts by at least ~100 times. Therefore, Ru-O-Ce sites of single-atom Ru/ceria catalysts are very active for NO oxidation. However, the corresponding single-atom Pt(Pd)-O-Ce are poor NO (and CO, for Pt [28-31, 69-71]) oxidation catalysts *due to inability of Pt and Pd to form a stable Metal-NO bond that would ensure coverage of NO when the interfacial O removal from M-O-Ce sites becomes favourable, as well as a spill-over of NO species onto the ceria support as nitrates*. Thus, Ru_1/CeO_2 stands out as the only ceria-supported material able to form thermally stable Ru-NO complexes.

To confirm the versatility of Ru/ceria materials for NOx related environmental catalysis, we now turn our attention to another challenging reaction *for gasoline engines* called NO reduction. TWC materials should perform catalytic removal of NOx in the presence of CO and water vapor under stoichiometric conditions [39-42]. We recently discovered that isolated Rh(I) ions on ceria can perform low temperature NO reduction by CO [42] effectively. We, therefore, wondered if Ru (which is ~ 60 times cheaper than Rh on the per-mass and per-molar basis) could also perform NO reduction by CO [69-71]. 0.5 wt% Ru/ceria sample is excellent for NO reduction by CO under dry conditions. Addition of water to the stream, in fact, does not lead to activity deterioration (Fig. 7, Fig.S16): in this case ammonia production is observed in significant amounts, due to Ru/ceria being an excellent water-gas-shift catalyst [42]. Decreasing Ru loading to 0.1 wt% also produces an active NO reduction catalyst, with excellent activity and full NO conversion ~185 °C. Thus, Ru_1/CeO_2 is an active catalyst for NO reduction by CO even at low Ru loading. TOF per Ru atoms ~ 370 hr^{-1} at 185 °C.

Although the Rh_1/CeO_2 has been investigated using ex-situ infrared spectroscopy, the mechanism of NO reduction by CO for a single-atom M_1/CeO_2 catalysts remains unexplored by in-situ methods. The reason behind this is the lack of structurally uniform and well-defined catalysts whose spectroscopic signatures could be unambiguously determined during the interaction with CO and NO molecules. With well-defined Ru_1/CeO_2 we now have an

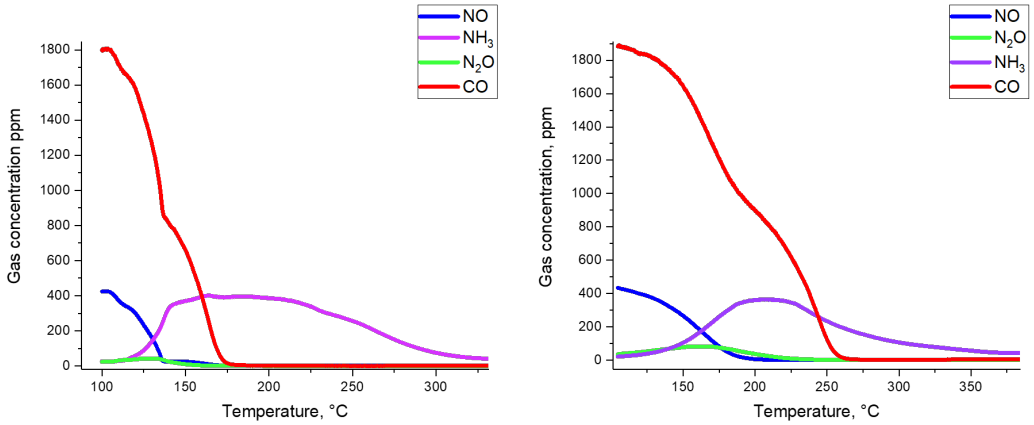

*Figure 7. NO reduction performance of 0.5 wt% Ru/CeO_2 (left graph) and 0.1 wt% Ru/CeO_2 (Right graph). 120 mg catalyst, 300 sscm/min total flow, GHSV ~ 150 L/G*hr, 470 ppm NO, 1850 ppm CO, ~3% H_2O balnaced in N_2. Performance of 0.5 wt% Ru/CeO_2 sample under dry conditions is shown in Fig. S16.*

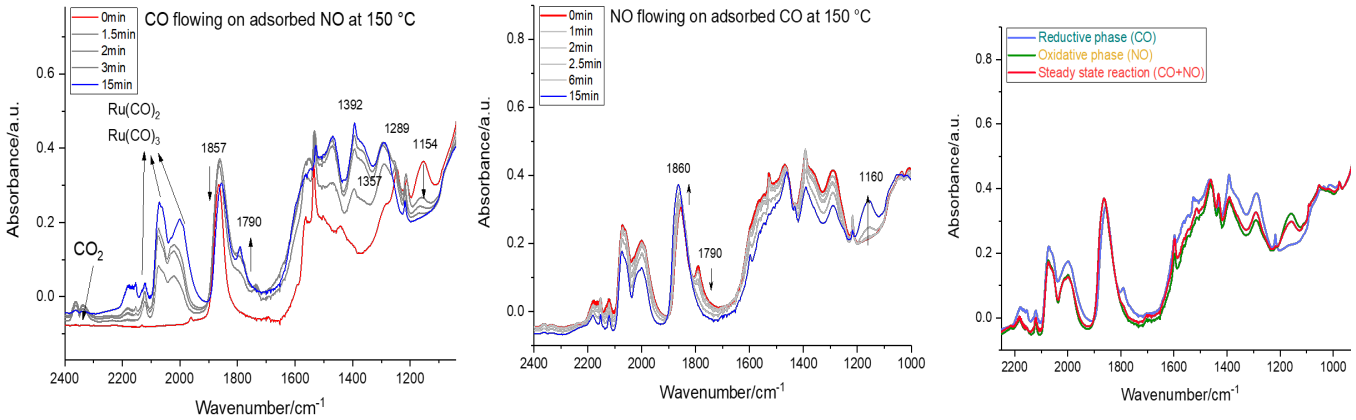

Figure 8. In-situ DRIFTS on 0.25 wt% Ru_1/CeO_2. A. Exposure to CO (2,500 ppm) of NO-saturated sample (saturated with 500 ppm NO flow for 30 minutes, then purged with He at 150 °C before exposure to CO) B. Subsequent exposure to NO flow after CO at 150 °C. C. Comparison of the Ru_1/CeO_2 during exposure to 2,500 ppm CO in the flow („reductive phase"), 500 ppm exposure to NO in the flow („oxidative phase"), and (500 pppm NO + 2,5000 ppm CO) exposure in the flow (steady state reaction; in the DRIFTS cell NO conversion ~ 30% under these conditions) at 150 °C

opportunity to explore the individual steps of NO reduction by CO: in order to do so, we employed excitation-modulation DRIFTS approach in our infra-red measurements: in short, at a temperature where (NO+CO) conversion occurs (150 °C), NO or CO pulses were applied to the system in antiphase for 3 consecutive cycles. The bands that appear/disappear in antiphase during these treatments indicate the appearance/consumption of the true catalytically active intermediates. Additionally, we performed in-situ DRIFTS with (NO+CO) flow at the same temperature (Figs 8, S17-S20).

During NO flow (~500 ppm) at 150 °C Ru-NO band at ~1860 cm^{-1} appears, as well as nitrite bands associated with ceria at ~1160 cm^{-1}. NO was then stopped, and CO flow started (2,500 ppm) (Fig. 8). Very dramatic changes were observed: nitrite band quickly decreased, simultaneously, Ce-O-Ru-NO band decreased with the concomitant evolution of the Ce-vacancy-Ru-NO band. Furthermore, the carbonate bands, easily attributable to poly- and mono-dentate carbonates, appeared (due to CO_2 evolution; some of which re-adsorbs on the surface at 150 °C). We then followed with NO treatment: NO treatment leads to the fast restoration of the Ru-NO band with the simultaneous healing of the oxygen vacancy; at the same time nitrite bands appears at 1160 cm^{-1}. Repetition of these NO-CO excitation-modulation cycles 3 times, allows to observe the phases that appear/disappear (respond dynamically during each cycle; Figs16-S20). The ones that are in anti-phase correspond to the active catalytic intermediates of the NO reduction by CO: indeed, during CO reduction: nitrites bands and Ru-NO bands are consumed with the formation of the oxygen vacancy between Ru(vacancy)Ce and CO_2 (carbonates). Treatment with NO, leads to re-filling of the oxygen vacancy with oxygen from NO and restoration of nitrite bands. We previously [] suggested based on ex-situ measurements that for Rh_1/CeO_2 CO reduces Rh(III) to Rh(I) (which we suggested to be the rate-limiting step of this reaction) with the following re-oxidation of Rh(I) with NO to Rh(III). Now, we show generally that we observe similar chemistry in-situ: but in this case, we prove the importance and direct participation of the oxygen vacancy between Ru and Ce in the catalysis: this vacancy is created by the process (1-5):

(1) CO-Ru-O-Ce → CO_2 + Ru (vac) Ce
(2) Ru (vac) Ce + 2 NO → NO-Ru (vac) Ce-NO → $Ru(N_2O_2)Ce$ → Ru-O-Ce + N_2O
(3) NO-Ru-O-Ce → Ru (vac) Ce-NO_2
(4) CO+ Ru (vac) Ce-NO_2 → CO-Ru Ce-NO_2 → CO_2 + Ru Ce-NO + NO → Ru (N_2O_2) Ce → Ru-O-Ce + N_2O

(5) Ru(vac)Ce + N_2O → O=N=N-Ru(vac)Ce → N_2 + Ru-O-Ce

The observation of the surface species during (NO+CO) flow over Ru/ceria sample in the DRIFTS cell (~30% NO conversion based on Mass-Spec data), and comparison with the states during NO and CO flows (Fig. 8), allows to conclude that during the reaction the surface remains mostly "oxidized". This is because the rate-limiting step is the removal of O between Ru-O-Ce by CO with the formation of CO_2: the subsequent steps (re-filling of the oxygen vacancy by NO) occur much faster, and during NO+CO flow we find basically mostly oxidized surface. However, the in-situ dynamic NO/CO experiment allowed us to clarify the mechanism as well as slow/fast steps of NO/CO reaction on atomically dispersed metal catalysts for the first time.

In summary, we discovered that Ru_1/CeO_2 catalysts show excellent performance for challenging NO_x pollutant abatement in both diesel and gasoline engines even at low metal loadings. We elucidated the location of active Ru(II) cations on the surface of ceria and provided molecular level understanding of the mechanism of NO oxidation, low-temperature NO storage and NO reduction by CO on these materials.

Acknowledgements

The research at PNNL was supported by the U.S. Department of Energy, Energy Efficiency and Renewable Energy, Vehicle Technology Office. Experiments were conducted in the Environmental Molecular Sciences Laboratory (EMSL), a national scientific user facility sponsored by the Department of Energy's Office of Biological and Environmental Research at Pacific Northwest National Laboratory (PNNL). PNNL is a multi-program national laboratory operated for the DOE by Battelle Memorial Institute under Contract DE-AC06-76RL01830. We acknowledge the support of CLEERS (Crosscut Lean Exhaust Emissions Reduction Simulations). CLEERS is an initiative funded by the U.S. Department of Energy (DOE) Vehicle Technologies Office to support the development of accurate tools for use in the design, calibration, and control of next generation engine/emissions control systems that maximize efficiency while complying with emissions regulations. HAA gratefully acknowledges the support by Bulgarian National Science Fund (project DN-19/2). GNV acknowledges the support of the project EXTREME, funded by the Bulgarian Ministry of Education and Science, D01-76/30.03.2021 through the programme "European Scientific Networks".

*Corresponding authors.

Conflict of interest

The authors filed for a patent.

(1) Royal College of Paediatrics and Child Health . Every breath we take—the lifelong impact of air pollution. London: Royal College of Paediatrics and Child Health, 2016.
(2) N. R. Jaegers, J. K. Lai, Y. He, E. Walter, D. A. Dixon, M. Vasiliu, Y. Chen, C. M. Wang, M. Y. Hu, K. T. Mueller, I. E. Wachs, Y. Wang, J. Z. Hu, Angew. Chem., Int. Ed., 2019, 131, 12739–12746.
(3) Ja-Hun Kwak, Russell G Tonkyn, Do Heui Kim, János Szanyi, Charles HF Peden, J. Catal., 2010, 275, 187-190.
(4) I. Bull, A. Moini, G. Koermer, J. Patchett, W. Jaglowski, S. Roth, US Patent US20070134146A1, 2010.
(5) Zones, S.I. US Patent 4 544 538, 1985.
(6) T. Seiyama, T. Arakawa, T. Matsuda, N. Yamazoe, and Y. Takita, Chem. Lett., 781 (1975)
(7) Chen, H.-Y.; Collier, J. E.; Liu, D.; Mantarosie, L.; Durán- Martín, D.; Novák, V.; Rajaram, R. R.; Thompsett, D. Catal. Lett. 2016, 146 (9), 1706–1711.
(8) Khivantsev, K.; Jaegers, N. R.; Kovarik, L.; Hanson, J. C.; Tao, F. (Feng); Tang, Y.; Zhang, X.; Koleva, I. Z.; Aleksandrov, H. A.; Vayssilov, G. N.; Wang, Y.; Gao, F.; Szanyi, J. Angew. Chem. 2018, 130 (51), 16914–16919.
(9) Khivantsev, K.; Jaegers, N. R.; Kovarik, L.; Prodinger, S.; Derewinski, M. A.; Wang, Y.; Gao, F.; Szanyi, J. Appl. Catal. A. Gen. 2019, 569, 141–148.
(10) Khivantsev, K.; Jaegers, N. R.; Koleva, I. Z.; Aleksandrov, H. A.; Kovarik, L.; Engelhard, M.; Gao, F.; Wang, Y.; Vayssilov, G. N.; Szanyi, J. J. Phys. Chem. C 2020, 124 (1), 309–321.
(11) Khivantsev, K.; Gao, F.; Kovarik, L.; Wang, Y.; Szanyi, J. J. Phys. Chem. C 2018, 122 (20), 10820–10827.
(12) Moliner, M.; Corma, A. React. Chem. Eng. 2019, 4 (2), 223–234.
(13) Khivantsev, K.; Jaegers, N. R.; Kovarik, L.; Hu, J. Z.; Gao, F.; Wang, Y.; Szanyi, J. Emiss. Control Sci. Technol. 2019. DOI: 10.1007/s40825-019-00139-w
(14) E. Bello, V. J. Margarit, E. M. Gallego, F. Schuetze, C. Hengst , A. Corma, M. Moliner, Microporous and Mesoporous Materials 302 (2020) 110222.
(15) K. Khivantsev, N. R. Jaegers, L. Kovarik, M. Wang, J. Z. Hu, Y. Wang, M. Derewinski, J. Szanyi, Chemrxiv 2020 DOI: 10.26434/chemrxiv.11821347
(16) Rajaram, R. R., Chen, H.-Y., Liu, D., US Patent US20150158019A1, 2015.
(17) Y. Ji, S. Bai and M. Crocker, Appl. Catal., B, 2015, 107–171 , 283-292.
(18) Ji, Y.; Xu, D.; Bai, S.; Graham, U.; Crocker, M.; Chen, B.; Shi, C.; Harris, D.; Scapens, D.; Darab, J. Ind. Eng. Chem. Res. 2017, 56, 111−125.
(19) K Khivantsev, J Szanyi, NR Jaegers, L Kovarik, F Gao, Y Wang, US Patent App. 16/546,641
(20) L. Castoldi, R. Matarrese, S. Morandi, P. Ticali, Luca Lietti, Catal. Today 2020 doi.org/10.1016/j.cattod.2020.02.019
(21) A. Porta, T. Pellegrinelli, L. Castoldi, R. Matarrese, S. Morandi, S. Dzwigaj, L. Lietti, Top. Catal. 61 (2018) 2021–2034.
(22) Y. Ji, S. Bai, D. Xu, D. Qian, Z. Wu, Y. Song, R. Pace, M. Crocker, K. Wilson, A. Lee, D. Harris, D. Scapens, App. Cat. B. 2019 doi: https://doi.org/10.1016/j.apcatb.2019.118499
(23) Ryou, Y. S.; Lee, J.; Cho, S. J.; Lee, H.; Kim, C. H.; Kim, D. Appl. Catal. B Environ. 2017, 212, 140–149.
(24) Ryou, Y. S.; Lee, J.; Lee, H.; Kim, C. H.; Kim, D. H., Catal. Today 2019, 320, 175–180.
(25) Lee, J.; Ryou, Y.; Hwang, S.; Kim, Y.; Cho, S. J.; Lee, H.; Kim, C. H.; Kim, D. H., Catal. Sci. Technol. 2019, 9 (1), 163–173.
(26) Kim, Y.; Hwang, S.; Lee, J.; Ryou, Y. S.; Lee, H.; Kim, C. H.; Kim, D. H. Emiss. Control Sci. Technol. 2019, 5 (2), 172–182.
(27) K. Khivantsev, X. Wei, L. Kovarik, N. R. Jaegers, E. D. Walter, P. Tran, Y. Wang, J. Szanyi, Chemrxiv 2020 DOI: 10.26434/chemrxiv.12385577
(28) Pereira-Hernandez, X. I.; DelaRiva, A.; Kunwar, D.; Xiong, H.; Sudduth, B.; Engelhard, M.; Kovarik, L.; Murayev, V.; Hensen, E.; Wang, Y.; Datye, A. K. Nat. Commun. 2019, DOI: 10.1038/s41467-019-09308-5
(29) Datye, A.; Wang, Y. Natl. Sci. Rev. 2018, 5, 630–632.

(30) Jones, J.; Xiong, H.; DeLaRiva, A. T.; Peterson, E. J.; Pham, H.; Challa, S. R.; Qi, G.; Oh, S.; Wiebenga, M. H.; Pereira Hernandez, X. I.; Wang, Y.; Datye, A. K. Science 2016, 353, 150−154.
(31) Nie, L.; Mei, D.; Xiong, H.; Peng, B.; Ren, Z.; Hernandez, X. I. P.; DeLaRiva, A.; Wang, M.; Engelhard, M. H.; Kovarik, L.; Datye, A. K.; Wang, Y., Science 2017, 358, 1419.
(32) Twigg, M.V., Haren Gandhi 1941-2010: Contributions to the Development and Implementation of Catalytic Emissions Control Systems. Platinum Metals Review, 2011. 55(1): p. 43-53.
(33) Warlimont, H.; W.E. Martienssen, eds. Springer Handbook of Condensed Matter and Materials Data. 2006.
(34) M. Koebel, M. Elsener, M. Kleemann, Catal. Today 59,335 (2000).
(35) N. Takahashi et al., Catal. Today 27, 63 (1996).
(36) M. Koebel, G. Madia, M. Elsener, Catal. Today 73, 239 (2002).
(37) P. Bourges, S. Lunati, G. Mabilon, Catalysis And Automotive Pollution Control IV 116, 213 (1998)
(38) C. H. Kim, G. Qi, K. Dahlberg, W. Li, Science, 327, pp. 1624-1627.
(39) Harrison, B, Diwell, AF, Hallett, C. Promoting platinum metals by ceria. Platinum Metals Rev1988; 32: 73–83.
(40) Taylor, K. Catal. Rev.: Sci. Eng. 1993, 35 (4), 457−481.
(41) Granger, P.; Parvulescu, V. I. Chem. Rev. 2011, 111.
(42) K. Khivantsev, C. Vargas, J. Tian, L. Kovarik, N. R. Jaegers, J. Szanyi, Y. Wang, Angewandte Chemie 133 (1), 395-402
(43) Hadjiivanov, K.; Lavalley, J.-C.; Lamotte, J.; Mauge, F.; SaintJust, J.; Che, M. J. Catal. 1998, 176, 415.
(44) H. Miessner, J. Am. Chem. Soc. 1994, 116, 11522-11530.
(45) Miessner, H.; Richter, K. J. Mol. Catal. A-Chem. 1999, 146, 107-115.
(46) Chen, H.-Y.; Collier, J. E.; Liu, D.; Mantarosie, L.; Durán- Martín, D.; Novák, V.; Rajaram, R. R.; Thompsett, D. Catal. Lett. 2016, 146 (9), 1706–1711.
(47) Chakarova K, Ivanova E, Hadjiivanov K, Klissurski D, Knozinger H (2004) Phys Chem Chem Phys 6:3702.
(48) J.Lee, J. Kim, Y. Kim, S. Hwang, H. Lee, C. H. Kim, D. H. Kim, Appl. Catal. B, 2020, 277, 119190
(49) K. Khivantsev, PhD Thesis, University of South Carolina, 2015.
(50) A.R. Derk, G.M. Moore, S. Sharma, E.W. McFarland, H Metiu, Top Catal 57, 118–124 (2014). https://doi.org/10.1007/s11244-013-0167-2A
(51) D. Chester, A. R. Derk, S. Sharma, H. Metiu, E. W. McFarland, Catal. Sci. Technol., 2015,5, 1783-1791
(52) M. Y. Mihaylov, V. R. Zdravkova, E. Z. Ivanova, H.A. Aleksandrov, P.St. Petkov, G.N. Vayssilov, K.I. Hadjiivanov, Journal of Catalysis 2020 https://doi.org/j.jcat.2020.06.015
(53) J. P. Perdew, J. A. Chevary, S. H. Vosko, K. A. Jackson, M. R. Pederson, D. J. Singh and C. Fiolhais, Phys. Rev. B, 1992, 46, 6671-6687;
(54) G. Kresse and J. Hafner, Phys. Rev. B, 1993, 47, 558-561.
(55) Version VASP.4.9; http://cms.mpi.univie.ac.at/vasp/
(56) G. Kresse and D. Joubert, Phys. Rev. B, 1999, 59, 1758-1775.
(57) V. I. Anisimov, F. Aryasetiawan and A. I. Lichtenstein, J. Phys.: Condens. Matter, 1997, 9, 767-808.
(58) S. L. Dudarev, G. A. Botton, S. Y. Savrasov, C. J. Humphreys and A. P. Sutton, Phys. Rev. B, 1998, 57, 1505-1509.
(59) C. Loschen, J. Carrasco, K. M. Neyman and F. Illas, Phys. Rev. B, 2007, 75, 035115.
(60) A. Migani, G. N. Vayssilov, S. T. Bromley, F. Illas and K. M. Neyman, Chem. Commun., 2010, 46, 5936-5938.
(61) A. Migani, G. N. Vayssilov, S. T. Bromley, F. Illas and K. M. Neyman, J. Mater. Chem., 2010, 20, 10535-10546.
(62) H. A. Aleksandrov, K. M. Neyman, and G. N. Vayssilov, Physical Chemistry Chemical Physics, 2015, 17, 14551–14560.
(63) H.A. Aleksandrov, K.M. Neyman, K.I. Hadjiivanov, G.N. Vayssilov, Physical Chemistry Chemical Physics, 2016 18 (32), 22108-22121
(64) I.Z. Koleva, H.A. Aleksandrov, G.N. Vayssilov, Catalysis Science & Technology, 2017 7 (3), 734-742
(65) G. N. Vayssilov, Y. Lykhach, A. Migani, T. Staudt, G. P. Petrova, N. Tsud, T. Skála, A. Bruix, F. Illas, K. C. Prince, K. M. Neyman, J. Libuda, Nature materials, 2011, 10 (4), 310-315.
(66) M. Capdevila-Cortada, N. López, Nature Materials 16 328–334 (2017)
(67) M. Capdevila-Cortada, G. Vilé, D. Teschner, J. Pérez-Ramírez, N. López, Applied Catalysis B: Environmental 197 299-312 (2015).
(68) N. Daelman, M. Capdevila-Cortada, N. López, Nature Materials 18 1215-1221 (2019)
(69) H Jeong, G Lee, BS Kim, J Bae, JW Han, H Lee, 2Journal of the American Chemical Society 140 (30), 9558-9565 (2018)
(70) H Jeong, J Bae, JW Han, H Lee, ACS Catalysis 7 (10), 7097-7105 (2019)
(71) H Jeong, O Kwon, BS Kim, J Bae, S Shin, HE Kim, J Kim, H Lee, Nature Catalysis 3 (4), 368-375 (2020)

Identification of single Ru(II) ions on ceria as a highly active catalyst for abatement of NOx pollutants

Konstantin Khivantsev,[a]*† Nicholas R. Jaegers,[a]† Hristiyan A. Aleksandrov,[b]†* Inhak Song,[a] Xavier Isidro Pereira-Hernandez,[a] Jinshu Tian[a], Libor Kovarik,[a] Georgi N. Vayssilov,[b] Yong Wang[a,c*] and János Szanyi[a]†*

Supplementary Information

Materials and Methods

Cerium nitrate hexahydrate was purchased from Sigma with purity of 99.999%. Ceria nanoparticles were prepared from it by heating in a regular muffle furnace under static conditions at 600 ^{0}C for 5 hours. Ruthenium nitrosyl nitrate solution was purchased from Sigma and used as is. To prepare the loadings of Ru on ceria of 0.1, 0.25 and 0.5 wt%, the desired amount of Ru precursor solution was dissolved in the minimum amount of water (total volume approximately equivalent to the pore of volume ceria) and added with a micropipette to the desired amount of ceria while continuously stirring with the spatula to ensure uniformity. The obtained wetted powder was dried under N_2 flow at 80 ^{0}C, and then calcined at 800 ^{0}C for 1 hour in a regular muffle furnace with a ramp rate of 5 ^{0}C/min. The as-prepared Ru/Ceria powders were pressed, crushed and sieved to 60-80 mesh, and subsequently used as catalysts. Samples with 0.5 and 1 wt% loading of Pd and Pt, respectively, were prepared in a way identical to the Ru/ceria sample. Pd and Pt tetramine nitrate salts (Sigma) were used as Pd and Pt precursors.

Na/SSZ-13 zeolite with Si/Al ~ 6 was hydrothermally synthesized using the following recipe: 0.8 g of NaOH (Sigma Aldrich, ≥ 99%) was dissolved in 50 ml of deionized water. Then, 17 g of TMAda-OH (Sachem Inc., 25% N,N,N-trimethyl-1-adamantyl ammonium hydroxide) was added as structure directing agent. Consequently, 1.5 g of $Al(OH)_3$ (Sigma Aldrich, ~54% Al_2O_3) was slowly added to the solution and stirred at 400 rpm until it was completely dissolved. Afterwards, 20.0 g of LUDOX HS-30 colloidal silica (Sigma Aldrich, 30 wt% suspension in H_2O) was added slowly to the solution until a uniform white gel was formed. The obtained gel was sealed in a 125 mL Teflon-lined stainless steel autoclave containing a magnetic stir bar. Hydrothermal synthesis was carried out at 160°C under continuous gel stirring at 400 rpm for 4 days. After synthesis, the zeolite cake was separated from the suspension by centrifugation and washed thoroughly with deionized water. It was then dried at 80°C under N_2 flow overnight and calcined in air at 550°C for 5 h in order to remove the SDA. NH_4/SSZ-13 was obtained by ion exchange

of the as-prepared Na/SSZ-13 zeolite with 0.5 M NH_4NO_3 solution at 80°C for 5 h. The process was repeated three times.

Pd/Zeolite powders with desired loading of Pd (1 wt%) was obtained via modified incipient wetness impregnation method, described by us earlier, with Pd(II) tetramine nitrate solution (10 wt %, Sigma) and NH_4-forms of zeolites. Benefits of using palladium (II) tetra-amine nitrate precursor versus palladium nitrate as well as NH_4-forms of zeolite were previously described in detail [8,11]. They were subsequently dried at 80ºC and subsequently calcined at 650ºC in static air. More specifically a minimum amount of the Pd(II) precursor solution was added to zeolite in the amount approximately equivalent to the total pore volume of the zeolite. The thick paste was mixed for 30 minutes, followed by calcination in air at 650°C for 5 h (ramping rate 2°C/min).

Diesel oxidation catalyst used for comparison of NO oxidation performance with Ru/Ceria catalyst was the commercial state-of-the-art diesel oxidation catalyst scraped off the real diesel aftertreatment system ("Cummins") fully compliant with the latest EPA Tier 4 Final and EU Stage IV emission standards. The powder was crushed and sieved to 60-80 mesh prior to testing.

Hydrothermal aging (HTA) was performed at 750 ºC for 10 hours in a flow reactor with GHSV ~ 150 L/g*hr. The gas mix, used for HTA, containing air and 10% H_2O in air.

(NO+CO) catalytic experiments were conducted in a plug-flow reactor system with powder samples (120 mg, 60–80 mesh) loaded in a quartz tube, using a synthetic gas mixture containing 460 ppm of NO and 1,750 ppm CO balanced with N_2 at a flow rate of 310 sccm (corresponding to GHSV 150 L/g*hr). Wet experiments were performed in the presence of 2.6 % water vapor. All the gas lines were heated to over 100 °C. Concentrations of reactants and products were measured by an online MKS MultiGas 2030 FTIR gas analyzer with a gas cell maintained at 191 °C. Two four-way valves were used for gas switching between the reactor and the bypass. Heating and cooling rates were 2 K/min.

Standard NOx adsorption tests were conducted in a plug-flow reactor system with powder samples (120 mg, 60–80 mesh) loaded in a quartz tube, using a synthetic gas mixture that contained ~200 ppm of NOx, CO (360 ppm), 14% O_2, 3% H_2O balanced with N_2 at a flow rate of 300 sccm at 100 ^{0}C. All the gas lines were heated to over 100 °C. Concentrations of reactants and products were measured by an online MKS MultiGas 2030 FTIR gas analyzer with a gas cell maintained at 191°C. GHSV for all the adsorption/desorption experiments was 150 L/g*hr. Heating rate was 10 K/min.

NO oxidation experiments were conducted in the same plug-flow reactor system in the presence and absence of water. 120 mg of desired catalyst were loaded, and the experiments were performed in the presence of 460 ppm NO, ~3% water, 13% O_2 balanced with nitrogen. Heating and cooling rates were 2 K/min.

BET surface areas were conducted on a Micromeritics ASAP-2000 instrument with Ar as the adsorbate. Prior to analysis, the samples were dehydrated under vacuum for 3 hours at 250 °C.

HAADF-STEM analysis was performed with an FEI Titan 80-300 microscope operated at 300 kV. The instrument is equipped with a CEOS GmbH double-hexapole aberration corrector for the probe-forming lens which allows for imaging with 0.1 nm resolution in scanning transmission electron microscopy mode (STEM). The images were acquired with a high angle annular dark field (HAADF) detector with inner collection angle set to 52 mrad. The powder samples were loaded into the sample holder. The images were collected in various projections and imaged immediately to minimize beam damage during the experiment.

DRIFTS experiments recorded on a Nicolet iS50R FTIR spectrometer at 4 cm^{-1} resolution. The spectrometer was connected to the mass-spectrometer for simultaneous monitoring of the gas effluent. The catalyst powder was packed into the DRIFTS cell and transferred to the cell where it was connected to the gas manifold and exposed to the flow of gases (NO, O_2, CO, He in desired concentrations – all of the gases ultra-high purity grade). Spectra were referenced to KBr background (at different temperatures) and 64 scans were averaged in each spectrum. Flow rates were ~150 L/g*hr.

The *in situ* transmission IR experiments were conducted in a home-built cell housed in the sample compartment of a Bruker Vertex 80 spectrometer, equipped with an MCT detector and operated at 4 cm^{-1} resolution. The powder sample was pressed onto a tungsten mesh which, in turn, was mounted onto a copper heating assembly attached to a ceramic feedthrough. The sample could be resistively heated, and the sample temperature was monitored by a thermocouple spot welded onto the top center of the W grid. The cold finger on the glass bulb containing CO was cooled with liquid nitrogen to eliminate any contamination originating from metal carbonyls, while NO was cleaned with multiple freeze–pump–thaw cycles. Prior to spectrum collection, a background with the sample in the IR beam was collected. Each spectrum reported is obtained by averaging 64 scans.

Computational method and models

The calculations are performed with periodic plane-wave density functional method using a GGA exchange-correlation functional PW91,[1] as implemented in VASP code.[2-4] An on-site Coulombic correction (U_{eff} = U-J)[5,6] is applied within the GGA+U scheme to all Ce atoms to obtain a localized description of Ce 4f-electrons in reduced Ce^{3+} ions. In line with previous studies[7,8] the U_{eff} value of 4.0 eV is used. A plane-wave basis with a 415 eV cut-off for the kinetic energy and projector-augmented wave[4] description of core-valence electron interactions are employed. Our model ceria nanoparticle $Ce_{21}O_{42}$ has a diameter of about 1 nm.[7,8] A cubic 2.0 × 2.0 × 2.0 nm unit cell is employed. Thus, each nanoparticle is separated from its periodically

repeated images in the neighboring unit cells in the three Cartesian directions by at least 0.9 nm to minimize interactions between the nanoparticles. Γ-point calculations are performed. Single-point total energy convergence tolerance at the self-consistency is set to 10^{-6} eV and structure optimizations continued until the maximum forces acting on each atom were less than 0.02 eV/Å. Where appropriate, spin-polarized calculations were performed in order to account for the reducibility of the Ce^{4+} ions.

The reported binding energies (BE) of the adsorbed NO on the Ru/ceria substrates are calculated as $BE = -E_{ad} - E_{sub} + E_{ad/sub}$, where E_{ad} is the total energy of the NO adsorbate in the gas phase, E_{sub} is the total energy of the corresponding Ru/ceria substrate system, and $E_{ad/sub}$ is the total energy of the substrate interacting with the NO adsorbate. With the above definition, negative values of BE imply favorable exothermic adsorption interaction.

Oxygen vacancy formation energies E_{vac} of the $RuO(NO)/Ce_{21}O_{42}$ complexes were calculated with respect to a half of the triplet-state energy of a free O_2 molecule $E(O_2)$:

$$E_{vac} = E(RuO(NO)/Ce_{21}O_{41}) + ½\, E(O_2) - E(RuO(NO)/Ce_{21}O_{42})$$

From the calculated energy values and vibrational frequencies we obtained the Gibbs free energies for the various ceria-containing models:

$\Delta G(RuO_X(NO)_m/Ce_{21}O_{42-Y}) = \Delta H(RuO_X(NO)_m/Ce_{21}O_{42-Y}) - T\Delta S(RuO_X(NO)_m/Ce_{21}O_{42-Y})$, where X = 0 or 1, m = 0 or 1, Y = 0 or 1.

The enthalpy values, $\Delta H(RuO_X(NO)_m/Ce_{21}O_{42-Y})$, were obtained from the electronic energies $E_{el}(RuO_X(NO)_m/Ce_{21}O_{42-Y})$ corrected for the internal vibrational energy E_v[9] and zero-point vibrational energy (ZPE) derived from all vibrational frequencies:

$H = E_{el} + E_v + ZPE$.

In the calculation of the entropy values of the $RuO_X(NO)_m/Ce_{21}O_{42-Y}$ structures only the electronic (S_{el}) and vibrational (S_v) degrees of freedom were taken into account.[10,11] For the NO, NO_2, and O_2 molecules in the gas phase translational and rotational contributions E_{tr} and E_{rot} were added to the internal energy and entropy:

$H = E_{el} + E_v + E_{tr} + E_{rot} + ZPE$,

$S = S_{el} + S_v + S_{tr} + S_{rot}$.

All the expressions for enthalpy and entropy contributions are available in Ref. 9.

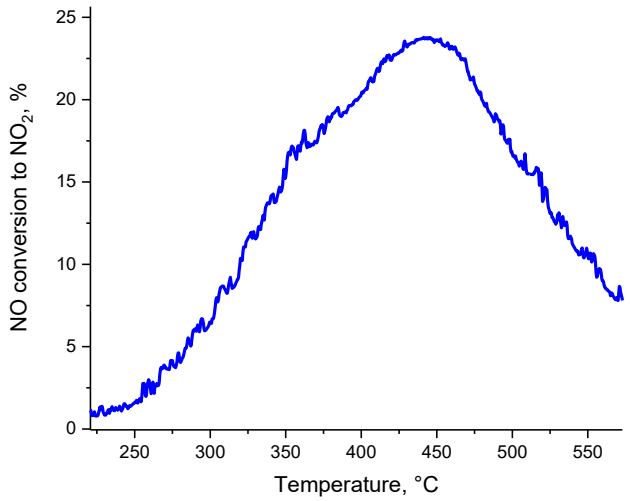

Figure S1. NO oxidation performance of 0.5 wt% Pd/CeO_2.120 mg catalyst, 300 sscm/min total flow, GHSV ~ 150 L/g*hr, 470 ppm NO, 13% O_2, balanced in N_2.

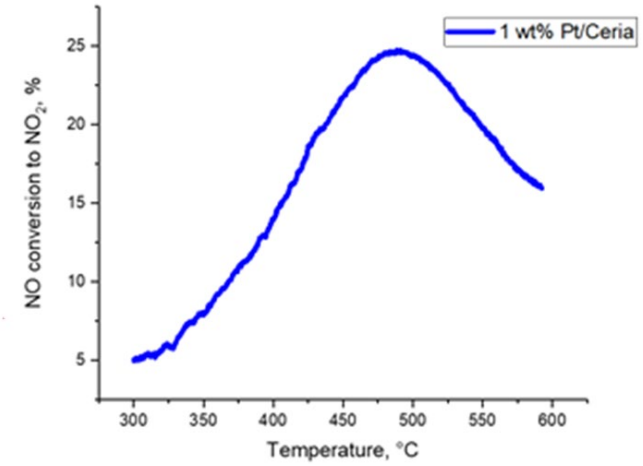

Figure S2. NO oxidation performance of 1 wt% Pt/CeO_2.120 mg catalyst, 300 sscm/min total flow, GHSV ~ 150 L/g*hr, 470 ppm NO, 13% O_2, balanced in N_2.

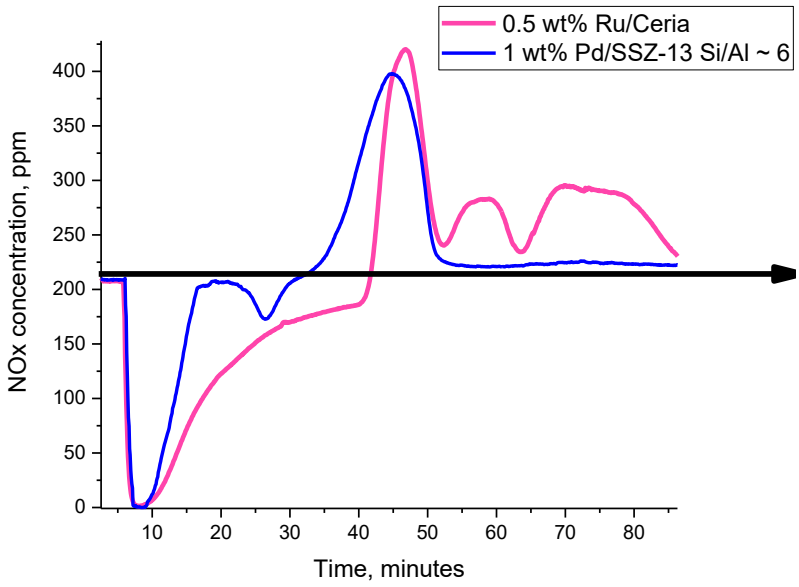

Figure S3. Comparison of PNA performance of 0.5 wt% Ru/Ceria and 1 wt% Pd/SSZ13 with Si/Al ~ 6. PNA was performed at 100 °C at GHSV ~ 150 L/g*h and conditions identical to Figs. 1 and 2. Note in the case of Pd/SSZ-13, ramp rate of 10 K/min was started at the 15 min mark, while for 0.5 wt% Ru/Ceria sample it was started at the 36 min mark.

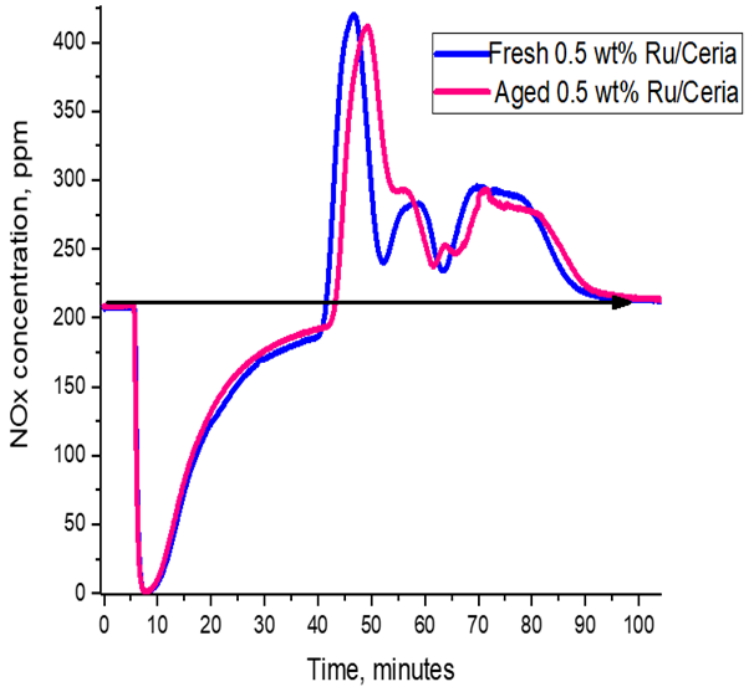

Figure S4. Comparison of PNA performance of 0.5 wt% Ru/Ceria before and after hydrothermal aging (the sample was aged at 750 °C in the flow of O_2/H2O and GHSV ~150 L/g*hr). PNA was performed at 100 °C at GHSV ~ 150 L/g*h and conditions identical to Fig. 3. Note in the case of fresh 0.5 wt% Ru/Ceria sample ramp rate (10 K/min) was started at the 36 min mark. For the aged sample, ramp was started at 37.5 min mark.

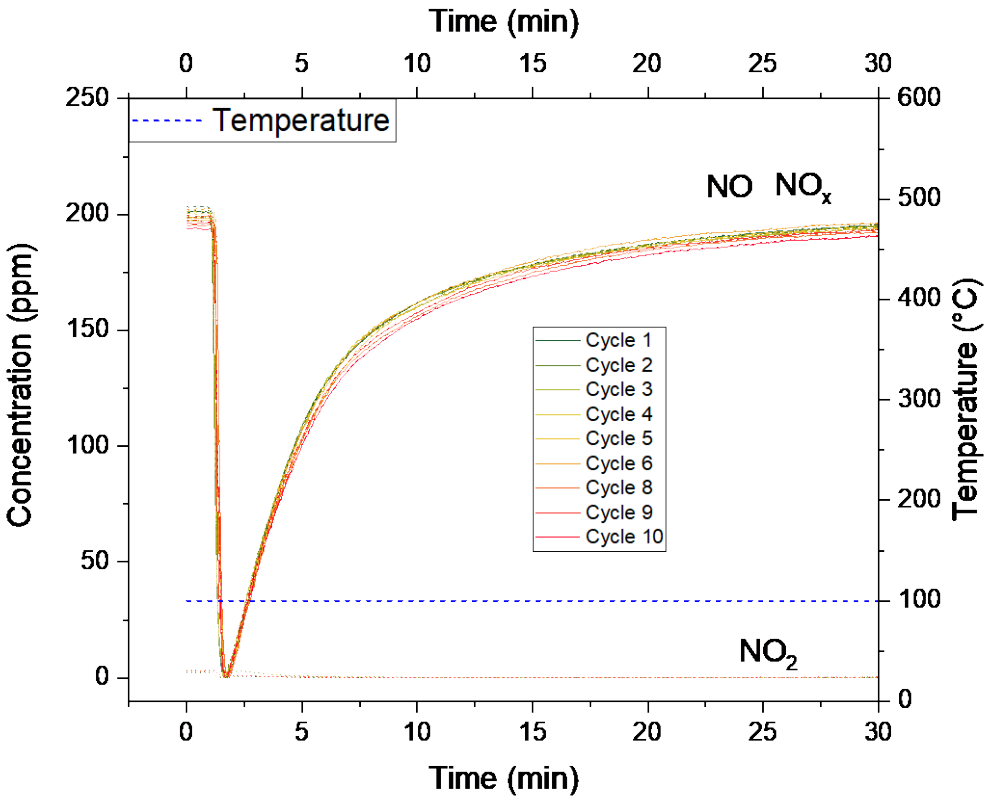

Figure S5. Adsorption part (30 minutes) for 10 consecutive cycles of NO adsorption over 0.25 wt% Ru_1/CeO_2 at 100 °C. GHSV ~ 150 L/g*hr. ~200 ppm NO, 2,000 ppm CO, 12% O_2, ~3 % H_2O.

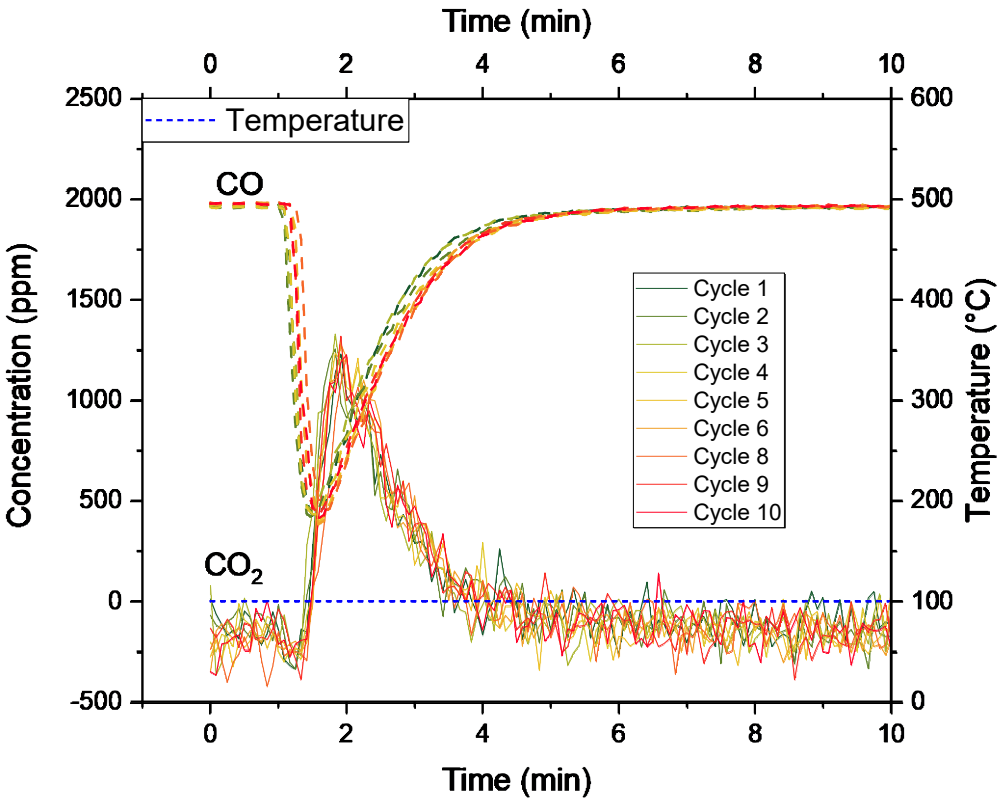

Figure S6. CO and CO_2 profiles during the adsorption part for 10 consecutive cycles of NO adsorption over 0.25 wt% Ru_1/CeO_2 at 100 °C. GHSV ~ 150 L/g*hr. ~200 ppm NO, 2,000 ppm CO, 12% O_2, ~3 % H_2O.

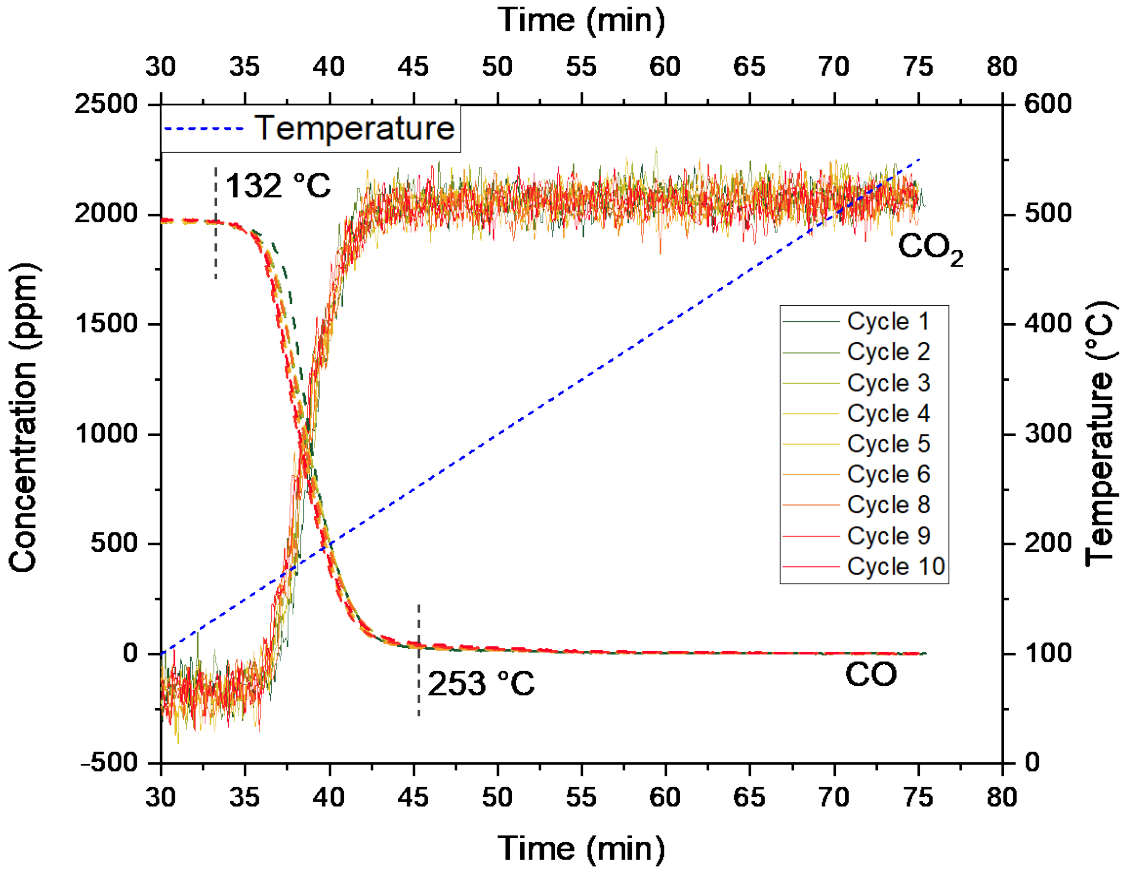

Figure S7. CO and CO_2 profiles during the adsorption part for 10 consecutive cycles of NO adsorption over 0.25 wt% Ru_1/CeO_2 at 100 ^{0}C. GHSV ~ 150 L/g*hr. ~200 ppm NO, 2,000 ppm CO, 12% O_2, ~3 % H_2O

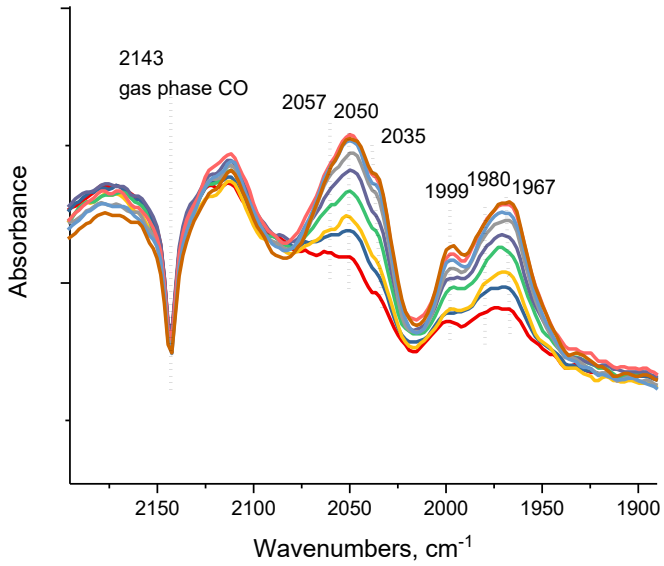

Figure S8. FTIR during CO adsorption (0.7 Torr equilibrium pressure) on 0.5 wt% Ru/ceria.

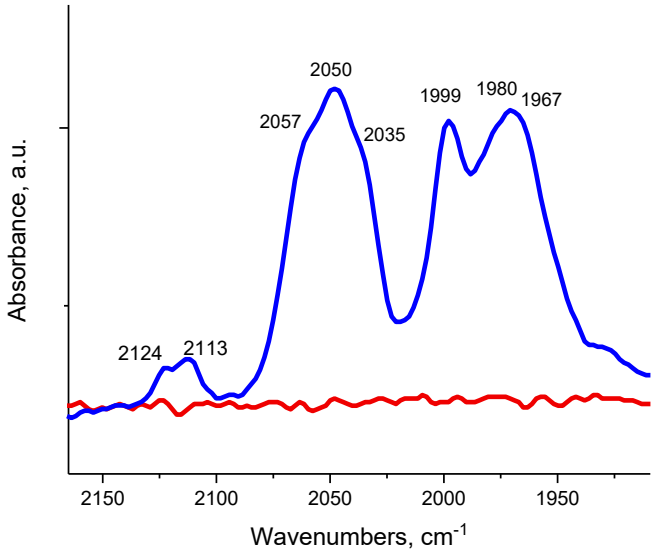

Figure S9. FTIR showing the CO region after applying high vacuum on the sample in Fig. S2. The bands at 2124 and 2113 cm^{-1}, obscured by the gas-phase CO bands in Fig. S2, are visible in this spectrum. The observed band-structure is very similar to Ru(II)/Zeolite system after CO adsorption, in which a mixture of di- and tri-carbonyls of Ru forms.

Continuous experiment for 0.25wt.% Ru/Ceria in DRIFTS cell

1. Pretreatment under O_2/He at 500C
1. Cooling to RT under He
2. $NO+O_2$ adsorption at RT
3. Heating from RT to 350C under $NO+O_2$ (To confirm temperature of NO oxidation)
4. Purging adsorbed species on catalyst with O_2/He at 350C, TPD from 350 to 500C (To confirm NO_2 formation)
5. Cooling to 200C under He
6. Sequential NO, $NO+O_2$ adsorption and subsequent purging with O_2/He at 200C
7. TPD from 200 to 500C under O_2/He

$NO+O_2$ adsorption on 0.25 wt.% Ru/Ceria at RT

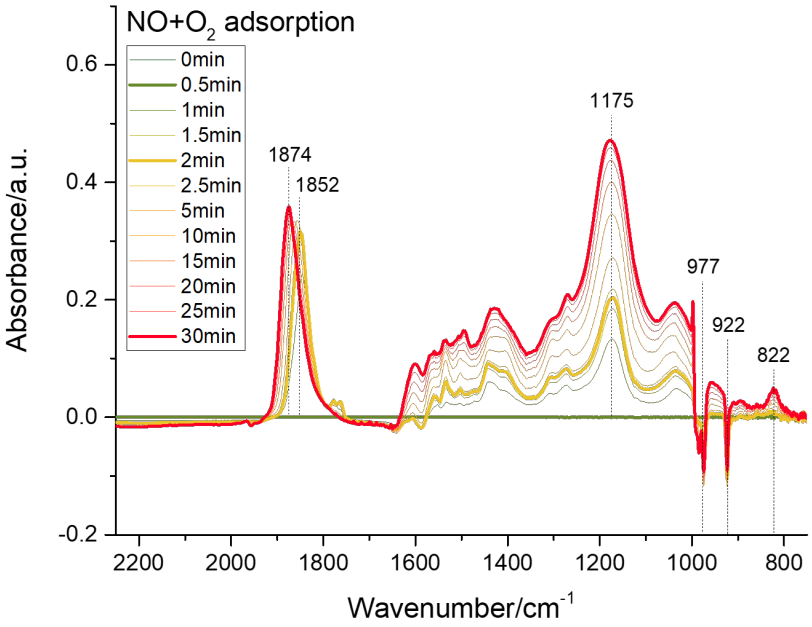

Figure S10. In-situ DRIFTS during flow of NO (500 ppm) and O_2 (12%) over 0.25 wt% Ru/ceria at room temperature. ~1170 cm^{-1} band is due to nitrite formation.

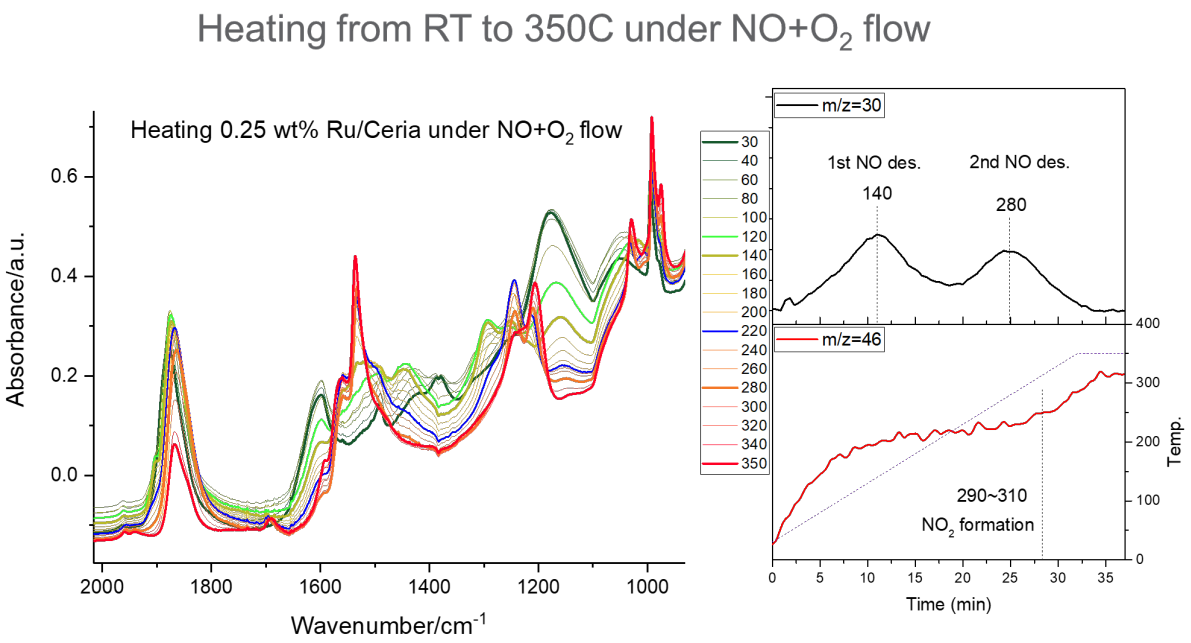

Figure S11. In-situ DRIFTS during flow of NO (500 ppm) and O_2 (12%) over 0.25 wt% Ru/ceria from room temperature to 350 ^{0}C coupled with Mass Spectroscopy measurements (GHSV ~ 150 L/g*hr). NO_2 formation occurs with a maximum at ~350 ^{0}C.

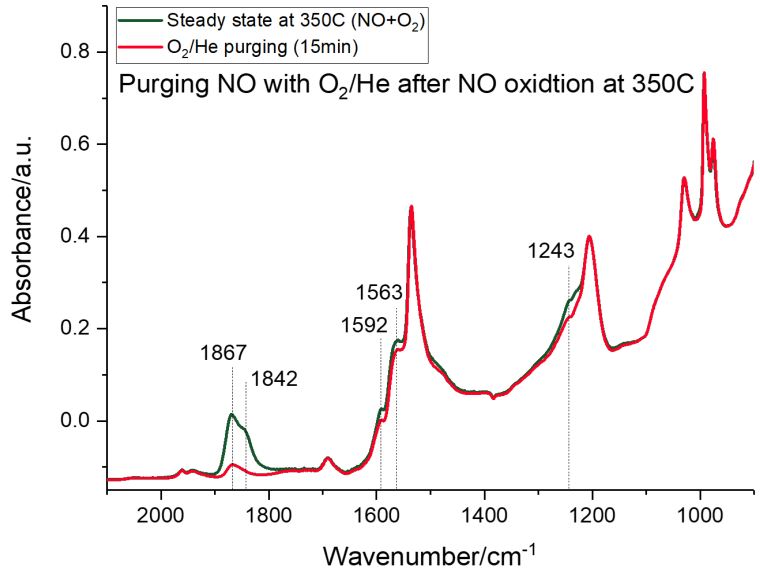

Figure S12. In-situ DRIFTS during flow of O_2 (12%) in He purge at 350 ^{0}C over 0.25 wt% Ru/ceria (GHSV ~ 150 L/g*hr).

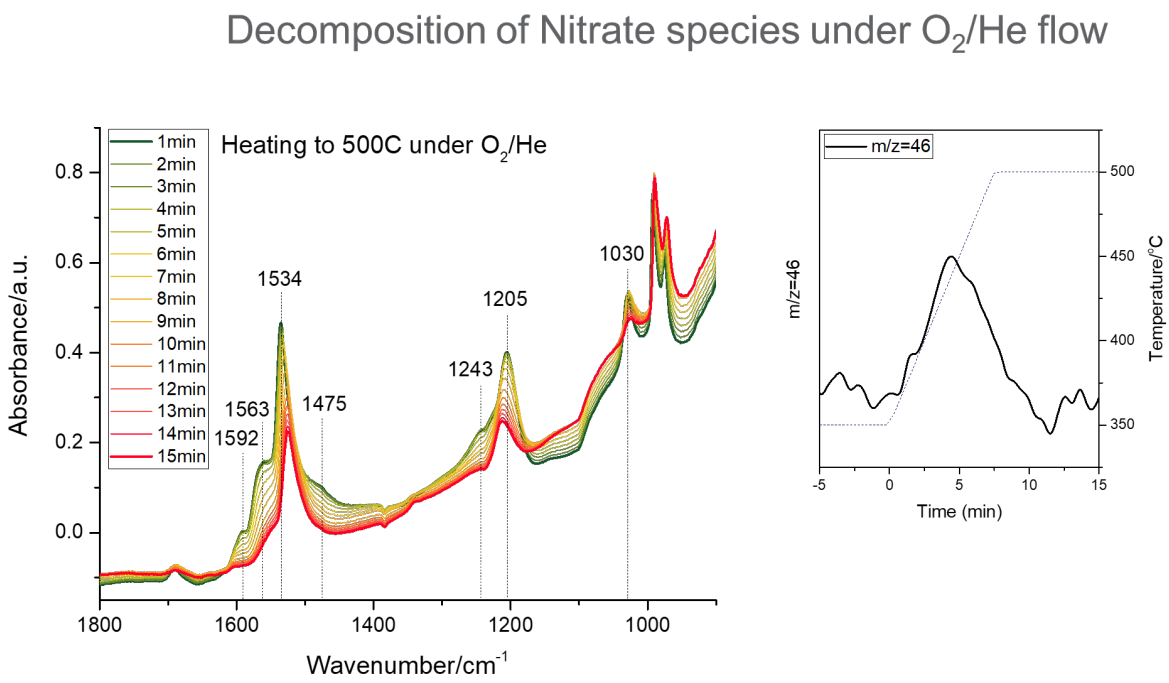

Figure S13. In-situ DRIFTS during flow of O_2 (12%) in from 350 °C to 500 °C over 0.25 wt% Ru/ceria (GHSV ~ 150 L/g*hr). NO_2 is formed during nitrate decomposition.

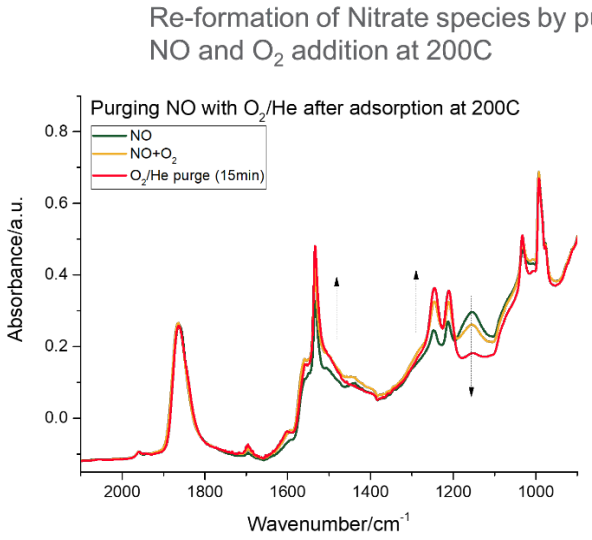

- Figure S14. In-situ DRIFTS at 200 °C over 0.25 wt% Ru/ceria (GHSV ~ 150 L/g*hr). After TPD to 500 °C (Fig. S13), catalyst was cooled to 200 °C under He flow, and subsequently exposed to the described gases sequentially.

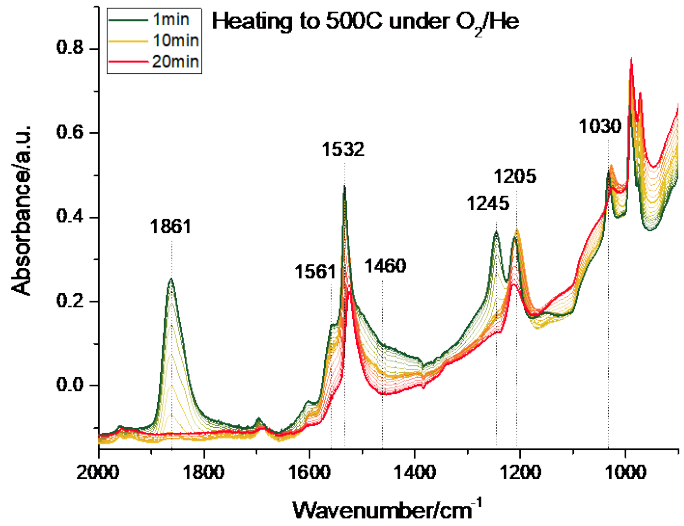

Figure S15. In-situ DRIFTS (after treatment in Fig. S14) from 200 to 500 °C over 0.25 wt% Ru/ceria (GHSV ~ 150 L/g*hr). NO_2 forms through nitrate decomposition

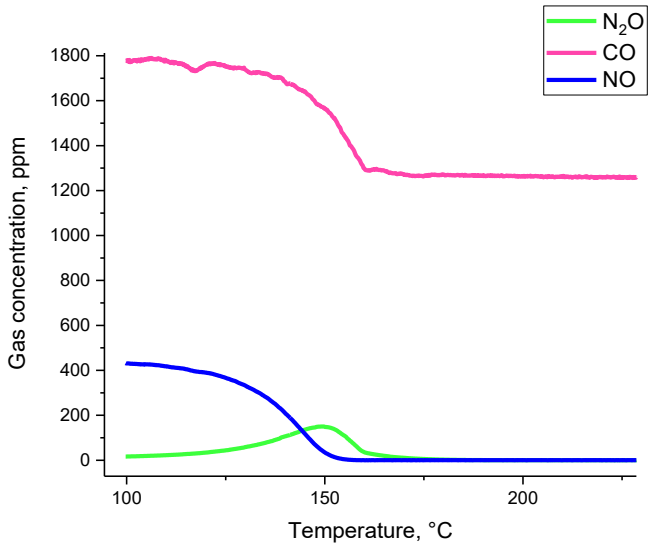

Figure S16. TWC performance of 0.5 wt% Ru_1/CeO_2 for dry CO+NO reaction. 120 mg catalyst, 300 sscm/min total flow, GHSV ~ 150 L/g*hr, 470 ppm NO, 1750 ppm CO, balanced in N_2.

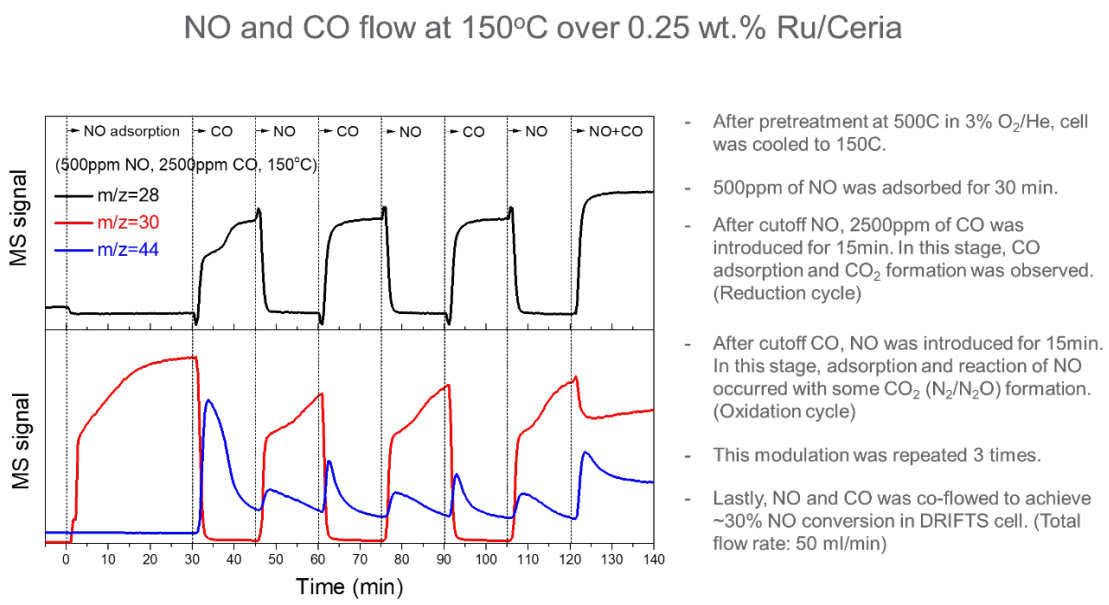

Figure S17. Summary of CO-NO excitation-modulation experiments over 0.25 wt% Ru_1/CeO_2 in the in-situ DRIFTS cell with effluent going into Mass Spectrometer. Those sequential experiments are presented in Figs. S18, Fig. 8 A and B (Main text)

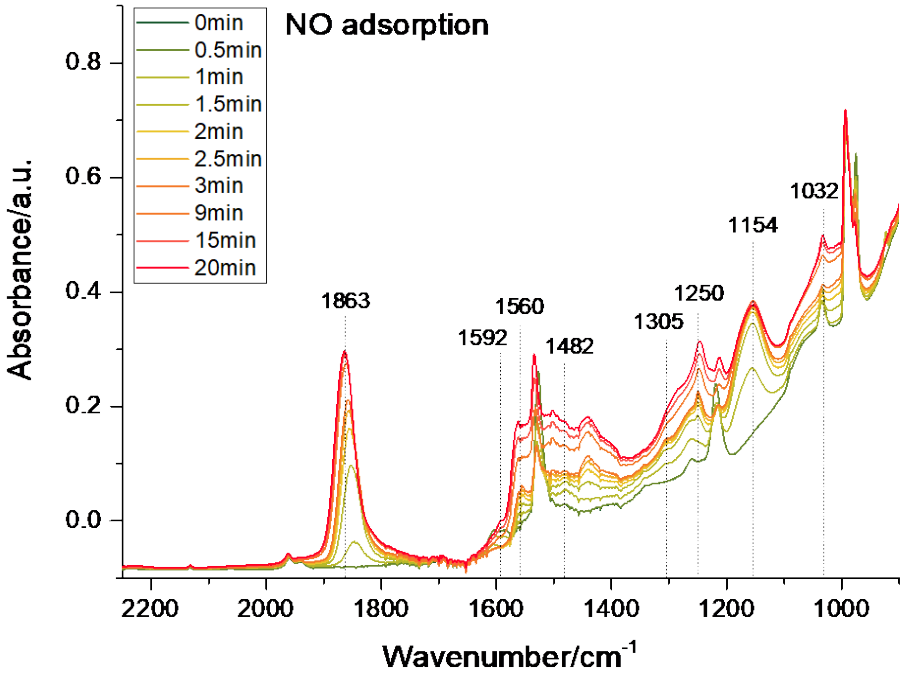

Figure S18 0.25 wt% Ru_1/CeO_2 in-situ DRIFTS during NO flow. *The 1st cycle of CO-NO* showing spectral modulations upon gas-phase changes is shown in Fig. 8 A and B (sequential experiments).

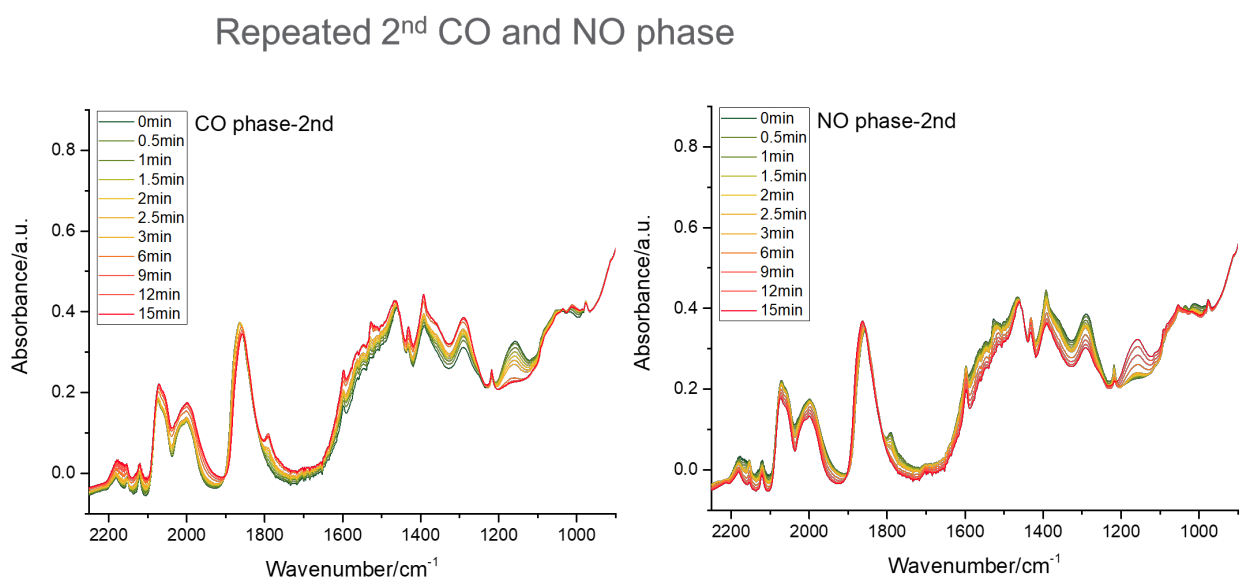

Figure S19. 0.25 wt% Ru_1/CeO_2 in-situ DRIFTS the 2nd cycle of CO-NO in-situ drifts showing spectral modulations upon gas-phase changes; those experiments were sequentially done after the experiment in Fig. 8B (the end of the 1st cycle).

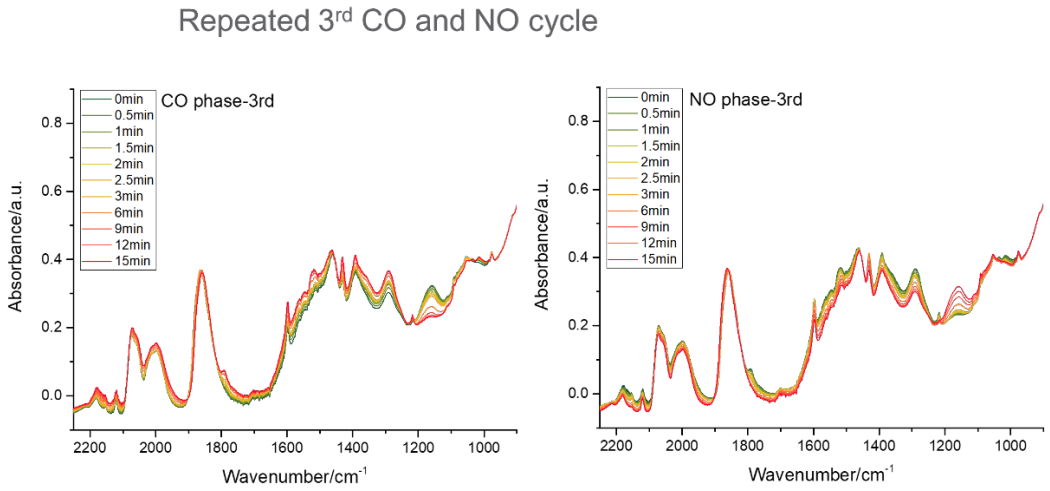

Figure S20. 0.25 wt% Ru_1/CeO_2 in-situ DRIFTS the 3rd cycle of CO-NO in-situ drifts showing spectral modulations upon gas-phase changes; those experiments were sequentially done after the last experiment in Fig. S18.

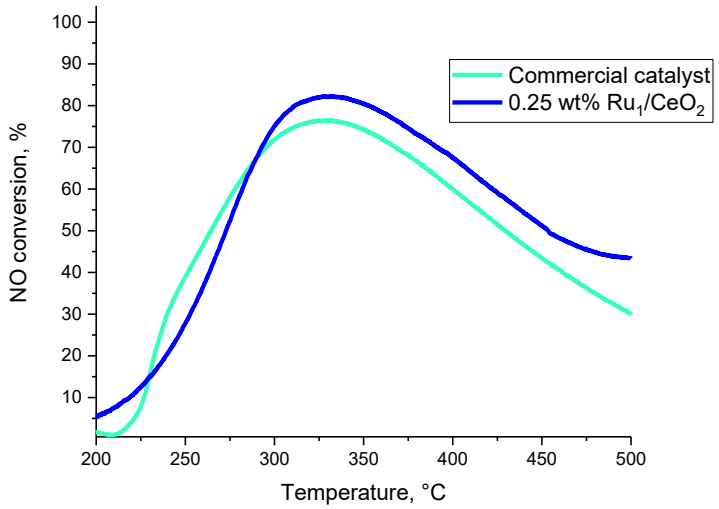

Figure S21. Comparison of NO oxidation performance of the commercial catalyst and 0.25 wt% Ru_1/CeO_2 (both catalysts were hydrothermally aged at 750 ºC in the presence of air/10% H_2O for 16 hours prior to measurements): 120 mg catalyst, temperature: starting at 500 ºC down to 200 ºC with a down-ramp of 2 K/min. ~200 ppm NO, 2,000 ppm CO, 12% O_2, ~3 % H_2O. GHSV 150 L/g*hr.

Table S1. BET Surface areas of various synthesized samples.

Sample	BET area, m^2/g
Ceria	98
Ceria calcined 800 °C	11
0.5 Ru/Ceria calcined 800 °C	44
1 Pt/Ceria calcined 800 °C	38
0.5 Pd/Ceria calcined 800 °C	36
0.1 Ru/Ceria calcined 800 °C	40

Table S2

Energetic and structural characteristics of the $RuO(NO)/Ce_{21}O_{42}$ and $RuO(NO)/Ce_{21}O_{41}$ complexes (i.e. without and with created O vacancy in the ceria support, respectively). Energy values are in eV, distances in pm, and vibrational frequencies in cm^{-1}.

$RuO(NO)/Ce_{21}O_{42}$	E_{rel}[a]	BE[b]	E_{vac}	N_s[c]	$N_s(Ru)$[d]	#(Ce^{3+})[e]	q(Ru)[h]	Ru-O	Ru-N	Δ(N-O)[f]	ν(N-O)[g]
a-1O_NO	1.72	-3.11		1	0.8	0	1	184;190	179	2.3	1763
b-1O_NO	2.91	-1.03		1	0.7	0	1	185;209;224	177	1.7	1799
c-1O_NO	1.42	-2.26		1	0.7	0	1	195;200;204	177	1.4	1824
d-1O_NO	1.91	-1.65		1	0.7	0	1	182;190	178	2.7	1733
e-1O_NO	0.00	-3.00		1	0	1	2	191;212;213; 213; 213	179	1.1	1840
e-1O_NO_vac_a	0.00		1.24	3	0.25	3	2	198;199;202; 204	173	2.4	1788
e-1O_NO_vac_b	2.08		3.32	1	0	3	2	192;212;212; 214; 215	178	1.2	1832
e-1O_NO_vac_c	0.63		1.86	1	0	3	2	191;212;212; 212; 213	178	1.1	1837

[a] Relative energy (in eV) with respect to the most stable structure in each series. [b] Binding energy (in eV) of the adsorbed NO ligand. [c] Number of unpaired electrons in the system. [d] Number of unpaired electrons in Ru. [e] Number of Ce^{3+} ions in the ceria nanoparticle. [f] Elongation of N–O bond upon adsorption with respect to the calculated bond length in gas-phase NO of 116.9 pm. [g] Calculated N-O vibrational frequencies. [h] Formal charge of Ru.

Table S3

Electronic and Gibbs free energies and barriers (given in parenthesis) of the reaction steps for NO oxidation on the most stable $RuO/Ce_{21}O_{42}$ complexes, e-1O and c-1O, where RuO species are located at the (100) and (111) facets of the $Ce_{21}O_{42}$ nanoparticle. All values are in kJ/mol.

Complex	e-1O	e-1O	c-1O	c-1O
Reaction step	$\Delta E(E^{\#})$	$\Delta G(G^{\#})$	$\Delta E(E^{\#})$	$\Delta G(G^{\#})$
$CeO_2/Ru + 1/2O_2 \rightarrow CeO_2/RuO$	-84	-73	-277	-229
$CeO_2/RuO + NO \rightarrow CeO_2/RuO(NO)$	-290	-88	-218	-80
$CeO_2/RuO(NO) \rightarrow CeO_2/Ru(NO_2)$	184 (249)	173 (200)	147 (182)	146 (154)
$CeO_2/Ru(NO_2) \rightarrow CeO_2/Ru + NO_2$	77	-73	236	101

1. J. P. Perdew, J. A. Chevary, S. H. Vosko, K. A. Jackson, M. R. Pederson, D. J. Singh and C. Fiolhais, *Phys. Rev. B*, 1992, **46**, 6671-6687; ibid. 1993, **48**, 4978-4978.
2. G. Kresse and J. Hafner, *Phys. Rev. B*, 1993, **47**, 558-561.
3. Version VASP.4.9; http://cms.mpi.univie.ac.at/vasp/
4. G. Kresse and D. Joubert, *Phys. Rev. B*, 1999, **59**, 1758-1775.

5. V. I. Anisimov, F. Aryasetiawan and A. I. Lichtenstein, *J. Phys.: Condens. Matter*, 1997, **9**, 767-808.
6. S. L. Dudarev, G. A. Botton, S. Y. Savrasov, C. J. Humphreys and A. P. Sutton, *Phys. Rev. B*, 1998, **57**, 1505-1509.
7. A. Migani, G. N. Vayssilov, S. T. Bromley, F. Illas and K. M. Neyman, *Chem. Commun.*, 2010, **46**, 5936-5938.
8. A. Migani, G. N. Vayssilov, S. T. Bromley, F. Illas and K. M. Neyman, *J. Mater. Chem.*, 2010, **20**, 10535-10546.
9. J. W. Ochterski, Thermochemistry in Gaussian, 2000, 1-19, www.gaussian.com/g_whitepap/thermo.htm
10. N. Hansen, T. Kerber, J. Sauer, A. T. Bell and F. J. Keil, *J. Am. Chem. Soc.*, 2010, **132**, 11525-11538.
11. H. A. Aleksandrov and G. N. Vayssilov, *Catal. Today*, 2010, **152**, 78-87.